Department of Mechanical and Manufacturing Engineering
Fibigerstræde 16
DK - 9220 Aalborg Øst
Phone +45 99 40 71 17
info@m-tech.aau.dk
www.m-tech.aau.dk/

Title:
Topology optimisation of the damping medium for an acoustic silencer

Semester:
4. M. Sc. in Design of Mechanical Systems

Project period:
02-02-2015 to 3-06-2015

ECTS:
30

Supervisors:
Sergey Sorokin
René Sørensen

Project group:
2.215-A

Rasmus Julsgaard

Håvard Borvik Kleppe

Daniel Rey Romero

Number printed: 6 pcs.
Number of pages: 54
Number of appendix: 2
Appendix CD

Synopsis:
This project focuses on the development of a topology optimisation tool for a dissipative muffler design in collaboration with *Lloyd's Register ODS*. The objective is to determine the optimal amount and placement of absorbing material required for a certain damping of the emitted sound. The initial stages of the report explains how the element type and element size is determined for a numerical model based on an analytical model of a simplified muffler design. The analytical model is developed based on the theory of linear acoustics and is used as a reference for the numerical model modelled in ANSYS®. When the element technology has been determined, the numerical model is modelled with the actual geometry. Damping material is added to the numerical model within a predefined design space and the elements are parametrised, allowing for manipulation of the material properties within each element. A thickness filter is applied to the design variables, which ensures a void-less design. The topology optimisation is conducted using a SLP solver. Several different tools are applied in the optimisation algorithm to ensure a robust algorithm. The final designs have provided great reduction of the damping material while still fulfilling the requirements for transmission loss.

Resumé

Denne specialeopgave er udført som den afsluttende del af kandidatuddannelsen Design af Mekaniske Systemer ved det Teknisk- Naturvidenskabelige Fakultet på Aalborg Universitet og i samarbejde med *Lloyd's Register ODS*. Opgaven omhandler research og udvikling af et topologi-optimeringsprogram i samspil med MATLAB og ANSYS® APDL til bestemmelsen af fordelingen af dæmpningsmateriale i et bestemt akustisk domæne.

Projektet er foreslået af *Lloyd's Register ODS* idet der fra dennes side ønskes en udvidelse af kompetencerne i feltet for topologi optimering af akustiske problemer. Intentionen er at kunne anvende optimeringsprogrammet til bestemmelse af generelle design regler for placering af dæmpningsmateriale i forskellige typer af lyddæmpere.

Udviklingen af optimeringsprogrammet tager således udgangspunkt i et eksisterende projekt angående designet af en lyddæmper med indbygget partikelfilter. Da pladsen i lyddæmperen er trang, ønskes det da at bestemme den minimale mængde dæmpningsmateriale krævet for at opnå en bestemt dæmpning af lyden ved tre specifikke frekvenser; 446 *Hz*, 892 *Hz* og 1338 *Hz*.

Lyddæmperen består af et 2.10 m langt rør med en diameter på 0.71 m. Åbning og udgang har ens hul-diameter på 0.24 m. Enderne af lyddæmperen er desuden udført med afrundede hjørner.

Første skridt i udviklingen af optimeringsprogrammet består i modelleringen af lyddæmperens akustiske felt uden tilføjet dæmpningsmateriale. Det akustiske felt er modelleret ved at anvende den lineære akustik teori på en simplificeret model af lyddæmperen, hvor de afrundede hjørner er erstattet af rette endeplader. Idet den lineære akustiske teori anvendes, antages det at der ingen interaktion er mellem det akustiske felt og strukturen omkring denne samt at inputtet ikke påvirkes af reflekterede bølger.

Den analytiske model er benyttet til at bestemme egen-frekvenser og tilhørende egenmodes, som anvendes til verifikation af en finite element model konstrueret i ANSYS® . Baseret på resultaterne fra den analytiske model fastsættes net kvaliteten samt element typen for finite element modellen, således fejlmargen mellem disse er tilfredsstillende. Transmissions tabet, eller dæmpningen, bestemmes ligeledes for den analytiske model og sammenlignes med finite element modellen. Der viste sig en god sammenhæng for transmissions tabet imellem modellerne ved frekvenser under 300 *Hz*, hvorefter det vurderes at ikke-linearitet, såsom interaktion med inputtet, begynder at påvirke transmission tabet.

En finite element model med korrekt geometri er efterfølgende konstrueret og udføres med de anbefalede værdier for net kvalitet og element type. Modellen udvides med inkludering af dæmpningsmaterialet ved brug af *Delany-Bazley* materialemodellen tilgængelig i ANSYS® .

Det vurderes at optimeringen må foretages ved brug af en 3D model med *Delany-Bazley*

materialemodellen, idet materialemodellen ikke er tilgængelig for 2D elementer, samt at transmissions tabet ikke kan forudsiges analytisk.

Lyddæmperen modelles med et manuelt defineret net og et design domæne defineres i 2D som efterfølgende projiceres omkring længdeaksen. Design domænet er bestående af 6 x 42 elementer i henholdsvis højden og længden. Hvert element i designdomænet tildeles en design variabel som skalerer materialeparameteren for flow-resistivitet σ i dæmpningsmaterialet mellem 0 og 1, således elementet opfører sig som henholdsvis luft eller dæmpningsmateriale.

For at muliggøre fremstilling af fordelingen af dæmpningsmaterialet, anvendes et tykkelsesfilter reformuleret af René Sørensen og Erik Lund [Sørensen and Lund, 2015] og oprindeligt udviklet af Fengwen Wang, Boyan Stefanov Lazarov og Ole Sigmund [Wang et al., 2011]. Tykkelses filteret sikrer at dæmpningsmaterialet påføres fra yderdiameteren af designdomænet og ind mod centrum af lyddæmperen, således at huller i fordelingen undgås.

Topologi-optimeringen er implementeret i MATLAB og baseres på et allerede eksisterende program af René Sørensen og Erik Lund [Sørensen and Lund, 2015], som benytter en Squential Linear Programming (SLP) algoritme til løsning af optimeringsproblemet.

Optimeringsprogrammet har leveret tilfredsstillende resultater for nedbringelsen af forbruget af dæmpningsmaterialet. Det er observeret, at placeringen af dæmpningsmaterialet har stor betydning for transmissions tabet gennem lyddæmperen. Det er også observeret at der udvises stor forskellighed i fordelingen af materialet hvis det ønskes at reducere materialeforbruget for hver enkel frekvens, i stedet for alle tre frekvenser på en gang. Start designet har endvidere også en stor betydning for det endelige resultat.

Designforslagene fra optimeringsprogrammet er dog ikke fuldkommen produktionsklar og kræver en vis mængde post-processering.

Preface

The following report is the result of a master these for the *Design of Mechanical Systems* (DMS), 2015 spring study programme, made in collaboration with *Lloyd's Register ODS*. The references in the appendix relies on the Harvard method, where the author and year are shown, example [Sørensen and Lund, 2015]. Pictures, equations and graphs are referred to by chapter number, example figure 1.1, equation (4.21), and chapter 1 *Introduction*.

The literature used for the report is placed in the bibliography at the end of the report.

The software applications used in the project are listed below:

- LaTeX for text editing
- MatLab for optimisation algorithm and graphs
- ANSYS® Classic APDL for FEM analysis
- Inkscape and Illustrator CS6 for creating figures
- Maple for various calculations

As an addition to the main report a CD is attached which contains a copy of the MatLab scripts, Maple scripts and ANSYS® input files. The CD is placed at the back of the appendix.

Contents

Introduction 1

This report is the documentation of a master thesis conducted at *Aalborg University* in collaboration with *Lloyd's Register ODS* about topology optimisation of a dissipative silencer. *Lloyd's Register ODS* is a marine society which focuses on developing safety and environmental standards for design, construction and operation of ships. It has been desired by *Lloyd's Register ODS* to extend its competencies to also include topology optimisation for acoustic problems. The development of a topology optimisation program for a dissipative silencer has therefore been appointed to this project group, in order to investigate the possibilities of acoustic topology optimisation. The topology optimisation tool has been developed by the authors of this report with help from Sergey V. Sorokin and Rene Sørensen.

The report explains the methods, techniques and theories used for solving the problem at hand. Results, conclusion and a discussion can be found in the back of the report.

1.1 Background

The silencer in question is attached to a screw compressor. The screw compressor runs at three pre-set velocities. When the screw compressor is active, large amounts of air is forced through an exhaust system. As the air leaves the system, sound is emitted. To prevent high amounts of noise from the system, a silencer is attached to the system. This will cancel out the loud noises which responsible for noise pollution or damage to the hearing.

1.2 Problem description

Lloyd's Register ODS provided the authors with a silencer design from a current silencer design project. Inside the silencer a particle filter must be fitted, which allows less room for the damping material. The silencer design is initialized by removing the current damping solution, but applying the existing silencer dimensions. The dimensions of the silencer can be seen on figure 1.1.

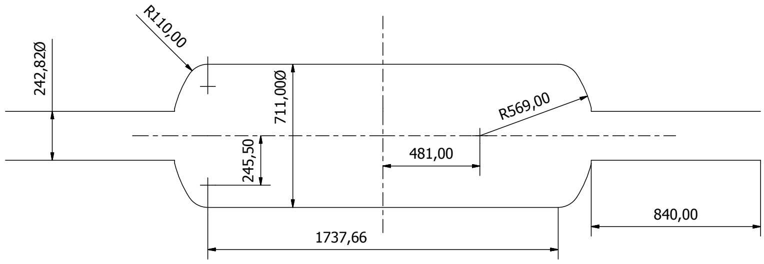

Figure 1.1: Dimensions of the silencer optimized in this project.

The three pre-set input frequencies are; 446 Hz, 892 Hz and 1336 Hz. The task is to develop a tool which can determine the minimum required damping material and its distribution while still damping the emitted sound to a set boundary of 17 dB.

1.3 Solution approach

To solve the problem formulated in section 1.2, four main steps were taken.

- Analytical investigation of eigenfrequencies and mode shapes of a simple model
- Implementation of real geometry and boundary conditions in FEM and investigation of transmission loss
- Introduction of damping material and investigation of transmission loss
- Topology optimisation of damping solution

The analytical investigation of the eigenfrequencies and mode shapes is performed to verify the numerical model. The theory of linear acoustics of a cylinder with fixed boundary conditions is well established and can be considered accurate. An accurate numerical model is developed by creating an analytical model to verify the elements and mesh size of the numerical model. When the elements and mesh size were determined the model is modified with real geometry and boundary conditions. The transmission loss is investigated to understand how much damping is required in the system. Damping material is added to the numerical model and transmission loss is investigated again. The damping material distribution and volume is optimised with topology optimisation using a *Sequential Linear Programming* solver. The solution process is visualized in figure 1.2.

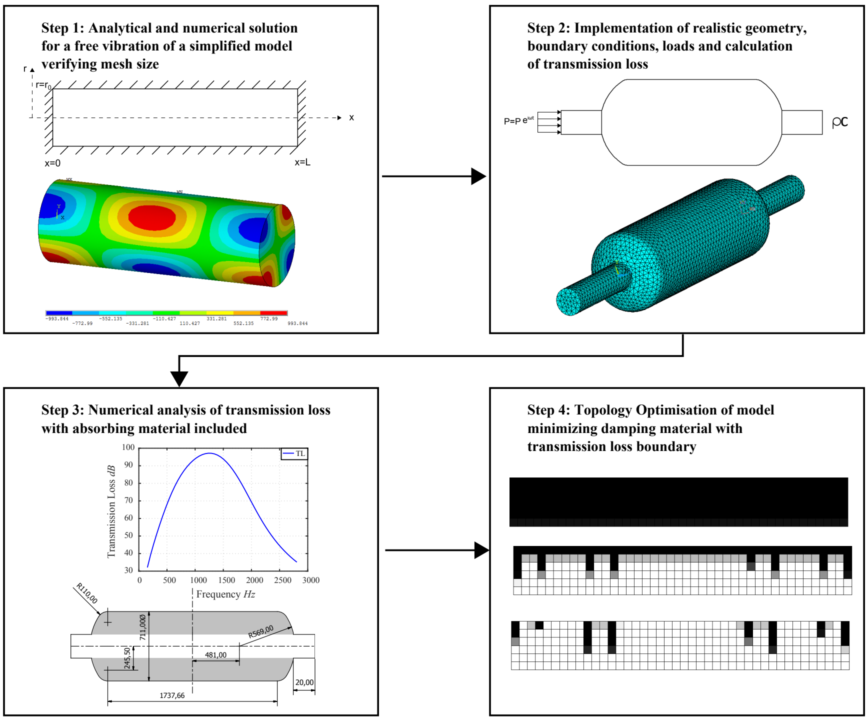

Figure 1.2: Flow chart showing the work process of the project.

The process is explained in details in this report ending with result discussions and conclusion.

Theory of linear acoustics 2

This chapter introduce the prerequisites needed to develop an analytical model. It covers the derivation of the governing equations needed to derive the wave equation. Later, the wave equation is used to describe the propagation of sound in a duct by introduction of the reduced wave equation also known as the *Helmholtz equation.* Finally the performance of a transmission line is examined with regards to the emitted sound power, which finally leads to the derivation of the transmission loss through a transmission line. The chapter will lay the foundation for the rest of the report as the notation, terminology and understanding of the physical behaviour of the silencer is presented herein and will be applied throughout the remaining chapters.

2.1 Governing equations

The governing equations sets up the rules for the physical system of the silencer by considering the physics of infinitesimal volumes of acoustic medium. The governing equations must secure that basic physical principles of the acoustic medium are obeyed, such as the conservation of mass and conservation of momentum, which will be discussed in the following.

2.1.1 Conservation of mass

The basic physical principle of conservation of mass is to secure continuity of the fluid. This implies that the amount of fluid (or mass) flowing into a certain volume must equal the amount of fluid exiting that volume. Fixed points in space are considered where the fluid might pass. The points are described by Cartesian coordinates x,y,z and time t is also considered. Consider now an infinitesimal volume dV. The mass of the volume is determined by the volume integral of the fluid density ρ.

$$\int \rho dV = m \tag{2.1}$$

The mass of flow out of the volume in unit time, is determined by the velocity of the fluid v and the surface area f.

$$\int \rho v df = \text{Mass of flow} \tag{2.2}$$

Note that the flow is positive if it is directed outward of the volume. As there is an outward flow, there must be a corresponding decrease of the mass inside the volume.

$$-\frac{\partial}{\partial t}\int \rho dV = \int \rho v df \tag{2.3}$$

The surface integral on the right side of equation (2.3) is converted to a volume integral by the Divergence theorem [Wendt et al., 1996] and is then inserted back into equation (2.3).

$$\int \rho v df = \int div(\rho v) dV \tag{2.4}$$

Where $div = \frac{\partial}{\partial x} + \frac{\partial}{\partial y} + \frac{\partial}{\partial z}$.

Rearranging equation (2.3) yields.

$$\int \left[\frac{\partial \rho}{\partial t} + div(\rho v) \right] dV = 0 \tag{2.5}$$

This condition must be valid for any volume, which is why the integral can be removed and the equation for conservation of mass is now obtained.

$$\frac{\partial \rho}{\partial t} + div(\rho v) = 0 \tag{2.6}$$

The second basic physical principal which must be valid for the fluid, the conservation of momentum, is considered next.

2.1.2 Conservation of momentum

The momentum of the fluid must be conserved as it enters and exits an infinitesimal volume element, as no energy can vanish. Consider the force acting on the surface of a volume element as the integral of pressure over the surface area. The force F can also be expressed as the gradient of the pressure over the volume element.

$$F = -\int p df = -\int \nabla p dV \tag{2.7}$$

Where $\nabla = \text{gradient} = i\frac{\partial}{\partial x} + j\frac{\partial}{\partial y} + k\frac{\partial}{\partial z}$.

The equation of motion for the volume element is established. Notice that the volume is considered as a unit volume.

$$\rho \frac{dv}{dt} = -\nabla p \tag{2.8}$$

Equation (2.8) considers a specific fluid particle as it moves about in space, but a formulation for fixed points in space is needed instead. Thus the derivative must refer to fixed points in space.

To enable this, consider the change in velocity dv from equation (2.8). It consists of a change in velocity during the time dt and a difference in velocity between two points in space, separated by a distance dr. The first part, the change in velocity during the time dt is expressed as

$$\left(\frac{\partial v}{\partial t} \right) dt \qquad \text{where} \qquad \frac{\partial v}{\partial t} \ \in \ x,y,z \tag{2.9}$$

The second part is the change in velocity between two points separated by a distance dr.

$$dx\frac{\partial v}{\partial x} + dy\frac{\partial v}{\partial y} + dz\frac{\partial v}{\partial z} = (dr \cdot \nabla)v \tag{2.10}$$

The two parts, equations (2.9) and (2.10) are combined in order to describe the change in velocity dv.

$$dv = \frac{\partial v}{\partial t}dt + (dr \cdot \nabla)v \tag{2.11}$$

Dividing both sides of (2.11) by dt and reducing, yields dv/dt of the equation of motion in equation (2.8).

$$\frac{dv}{dt} = \frac{\partial v}{\partial t} + (v \cdot \nabla)v \tag{2.12}$$

Equation (2.12) is inserted into the equation of motion for the particle (2.13) and is reduced to the final expression for the conservation of momentum (2.14).

$$\rho \left(\frac{\partial v}{\partial t} + (v \cdot \nabla)v \right) = -\nabla p \tag{2.13}$$

$$\Downarrow$$

$$\frac{\partial v}{\partial t} + (v \cdot \nabla)v = -\frac{1}{\rho}\nabla p \tag{2.14}$$

As the governing equations have now been derived, they are in the following section, applied as the basis for the derivation of the wave equation.

2.2 Derivation of wave equation

The wave equation describes the distribution of pressure and velocity throughout the acoustic system. It is derived using the governing equations that has just been determined.

In order to derive the wave equation, it is required that mass and momentum is conserved for an infinitesimal volume, meaning that the governing equations are applied.

$$\textit{Conservation of mass:} \qquad \frac{\partial \rho}{\partial t} + div(\rho v) = 0 \tag{2.15}$$

$$\textit{Conservation of momentum:} \qquad \frac{\partial v}{\partial t} + (v \cdot \nabla)v = -\frac{1}{\rho}\nabla p \tag{2.16}$$

Viscosity of the fluid is neglected, as only air is considered as the acoustic medium in this report. The governing equations are simplified by the introduction of a very small disturbance to the density and pressure, as seen in equations (2.17) and (2.18).

$$\rho = \rho_0 + \rho' \qquad \rho_0 >> \rho' \qquad \rho_0 = constant \tag{2.17}$$

$$p = p_0 + p' \qquad p_0 >> p' \qquad p_0 = constant \tag{2.18}$$

A relation between the pressure and density perturbations is now defined.

$$p' = c_0^2 \rho' \tag{2.19}$$

Where c_0 is the speed of sound in the acoustic medium.

The conservation of momentum is further simplified by assuming that the velocity in the fluid is so small that the non-linear term can be neglected.

$$\frac{\partial v}{\partial t} + (v \cdot \nabla)v \approx \frac{\partial v}{\partial t} \tag{2.20}$$

The assumptions above are now introduced to the governing equations for mass and momentum conservation, yielding equations (2.21) and (2.22) respectively.

$$\frac{1}{c_0^2}\frac{\partial p'}{\partial t} + \rho_0 div(v) = 0 \tag{2.21}$$

$$\frac{\partial v}{\partial t} = -\frac{1}{\rho_0}\nabla p' \tag{2.22}$$

The velocity potential φ is now introduced as $v = \nabla\varphi$, which rewrites the equation for conservation of momentum.

$$\nabla\left(\frac{\partial\varphi}{\partial t} + \frac{1}{\rho_0}p'\right) = 0 \tag{2.23}$$

For the left-hand side of equation (2.23) to be equal to zero, it must hold that $\frac{\partial\varphi}{\partial t} + \frac{1}{\rho_0}p' =$ constant. The constant represents the reference level of the acoustic pressure p' and equating this to zero yields.

$$p' = -\rho_0\frac{\partial\varphi}{\partial t} \tag{2.24}$$

Inserting the expression for the pressure perturbation into the conservation of mass (2.21) and the wave equation is finally derived as equation (2.26).

$$-\frac{1}{c_0^2}\frac{\partial^2\varphi}{\partial t^2} + div(\nabla\varphi) = 0 \tag{2.25}$$

$$-\frac{1}{c_0^2}\frac{\partial^2\varphi}{\partial t^2} + \Delta\varphi = 0 \tag{2.26}$$

Where Δ is the Laplace operator. The Laplace operator is shown for Cartesian and cylindrical coordinates in equations (2.27) and (2.28) respectively.

$$\Delta = \frac{\partial^2}{\partial x^2} + \frac{\partial^2}{\partial y^2} + \frac{\partial^2}{\partial z^2} \tag{2.27}$$

$$\Delta = \frac{\partial^2}{\partial r^2} + \frac{1}{r}\frac{\partial}{\partial r} + \frac{1}{r^2}\frac{\partial^2}{\partial\theta^2} + \frac{\partial^2}{\partial z^2} \tag{2.28}$$

2.2.1 Reduced wave equation

As the general wave equation has been derived, it is now transformed into a time-harmonic domain. The time-harmonic domain simplifies the wave equation dramatically as the excitation is no longer arbitrary (which the wave equation supports) but instead purely harmonic. This implies that the velocity potential φ of the wave equation is formulated as a time-harmonic function.

$$\varphi = \widetilde{\varphi}e^{\pm i\omega t} \tag{2.29}$$

With this formulation for the velocity potential, the wave equation transforms to the Helmholtz equation also known as the reduced wave equation.

$$\Delta\widetilde{\varphi} + \frac{\omega^2}{c_0^2}\widetilde{\varphi} = 0 \tag{2.30}$$

The physical variables are expressed in harmonic time domain as well.

$$\vec{v} \equiv \widetilde{\vec{v}}e^{\pm i\omega t} \tag{2.31}$$

$$p \equiv \widetilde{p}e^{\pm i\omega t} \tag{2.32}$$

From equation (2.24) the relation between pressure and velocity potential reduce to an algebraic equation.

$$\widetilde{p} = \mp i\rho_0\omega\widetilde{\varphi} \tag{2.33}$$

2.2.2 Boundary conditions

In order to solve the Helmholtz equation, which is a second order differential equation, two boundary conditions must be supplied. One condition is applied to the surface of the source called S_1, located inside an acoustic volume. The source vibrates with a velocity amplitude of V_0 normal to its surface. The sign convention is now readily defined as positive if the velocity of the source is directed away from the acoustic volume. The boundary on the source is thus defined as the velocity vector $\vec{\tilde{v}}$ in the normal direction of the source surface, see equation (2.34).

$$v_n \equiv \vec{n} \cdot \vec{\tilde{v}} = \frac{\partial \varphi}{\partial n} = -V_0 \tag{2.34}$$

Consider now the second boundary condition surrounding the acoustic volume. Several different formulations can be used according to physical behavior of the boundary. For a completely rigid boundary S_2, the velocity of a fluid particle at the boundary must equate to zero as in equation (2.35).

$$v_n = 0 \tag{2.35}$$

Contrary to the condition of equation (2.35) is an acoustically soft boundary, S_3. Here no acoustic pressure is developed, see equation (2.36). The velocity potential can be used to describe this boundary condition as well, according to equation (2.33). This is also known as a pressure release boundary.

$$\widetilde{p} = 0 \tag{2.36}$$

$$\widetilde{\varphi} = 0 \tag{2.37}$$

The third case, S_4, is of a boundary which is neither completely rigid or completely compliant with regards to the pressure. This type of boundary is called an impedance boundary and basically determines the relation between pressure and velocity.

$$\widetilde{p} = Z\widetilde{v}_n \tag{2.38}$$

Where Z is a local impedance of the boundary which can be of complex-value. Applying equations (2.33) and (2.34) the impedance boundary can be described in terms of the velocity potential.

$$\mp i\rho_0\omega\widetilde{\varphi} = Z\frac{\partial \widetilde{\varphi}}{\partial n} \tag{2.39}$$

2.2.3 Plane waves

Consider a one-dimensional case of a propagating wave. In one-dimensional space, the propagation is referred to as a plane wave propagation. It is useful to consider the propagation of the wave in one dimension as the direction of the wave can be established more easily. The Helmholtz equation is reduced to equation (2.40) for one dimensional space.

$$\frac{\partial^2 \widetilde{\varphi}}{\partial x^2} + \frac{\omega^2}{c_0^2}\widetilde{\varphi} = 0 \tag{2.40}$$

If the case of an infinite cylinder, with a piston in one end as the excitation source, the boundary condition for the source based on equation (2.34) is formulated in equation (2.41). Notice the change of the sign for V_n.

$$\frac{\partial \widetilde{\varphi}}{\partial x} = V_n \tag{2.41}$$

The solution to the one dimensional problem of equation (2.40) is given in equation (2.42), as the general solution to a homogeneous second order differential equation.

$$\widetilde{\varphi} = A_1 e^{i\frac{\omega}{c_0}x} + A_2 e^{-i\frac{\omega}{c_0}x} \tag{2.42}$$

As seen from equation (2.42) two constants are to be determined, but only one boundary condition have been applied as the cylinder is assumed to be infinitely long. This means that the waves will only propagate away from the source and will never be reflected back towards the source. The choice of the time dependence formulation in equation (2.29) determines which constant will describe the wave propagation. If $e^{i\omega t}$ is used, the positive wave propagation (away from the source), is determined by A_2 while $A_1 = 0$ as the wave cannot propagate into the source. On the contrary, if $e^{-i\omega t}$ is applied, the positive direction of the wave propagation is handled by A_1 and now $A_2 = 0$.
In the following, the time dependence will be expressed as $e^{-i\omega t}$.

The solution to the reduced wave equation in one dimension is thus only containing the term with A_1.

$$\widetilde{\varphi} = A_1 e^{i\frac{\omega}{c_0}x} \tag{2.43}$$

To determine A_1, the boundary condition at the source at $x = 0$ is applied.

$$\frac{d\widetilde{\varphi}}{dx} = i\frac{\omega}{c_0}A_1 = V_0 \qquad \Rightarrow \qquad A_1 = -\frac{ic_0}{\omega}V_0 \tag{2.44}$$

Inserting the expression for A_1 back into equation (2.43) the final expression for the velocity potential arise.

$$\widetilde{\varphi} = -\frac{ic_0}{\omega}V_0 e^{i\frac{\omega}{c_0}x} \tag{2.45}$$

By applying equations (2.33) and (2.44), formulations for pressure and velocity in the acoustic field are derived.

$$\widetilde{v}_x = V_0 e^{i\frac{\omega}{c_0}x} \tag{2.46}$$

$$\widetilde{p} = i\rho_0\omega\widetilde{\varphi} = \rho_0 c_0 V_0 e^{i\frac{\omega}{c_0}x} \tag{2.47}$$

Equations (2.45), (2.46) and (2.47) gives the solution to the propagation of plane waves.

The ratio between pressure and velocity at any point in the one dimensional space and at any instant of time is called the characteristic impedance of the plane wave, as shown in equation (2.48). It is derived from equations (2.46) and (2.47).

$$Z_0 = \frac{\widetilde{p}}{\widetilde{v}_x} = \rho_0 c_0 \tag{2.48}$$

The characteristic impedance can be interpreted as the unobstructed resistance to the sound as it moves in the one dimensional acoustic medium. It will later be applied as boundary conditions at the inlet and outlet in the modelling of the muffler and in the following section when transmission loss must be determined.

2.3 System performance

The system performance is in the following used a term to describe the amount of sound emitted from any given system. First the emitted sound power is considered, as this describes the amount of energy transferred trough a system. Next the transmission loss is considered as the energy lost in a system and the prerequisite for an analytical transmission line model is discussed.

2.3.1 Emitted sound power

The sound wave transports energy from the source, say a piston, to infinity. The average power over one excitation is usually used to describe the sound power of a given system. Consider an infinitely long tube as before, with a piston in one end. The sound power for this case is shown in equation (2.49) [Sorokin].

$$N = \frac{1}{2}\mathrm{Re}\left[\frac{1}{T}\int_{t_0}^{t_0+T}\int_A p^{'} v^* dA dt\right] \tag{2.49}$$

Where A is the cross sectional area of the tube, $T = \frac{2\pi}{\omega}$ is the period of the excitation and v^* is the complex conjugate of the velocity.

By assuming plane waves and applying the formulations for acoustic pressure and velocity from equations (2.46) and (2.47), combined with the formulation for velocity and pressure in harmonic time domain from equations (2.31) and (2.32), the pressure and velocity can be rewritten.

$$p^{'} = \rho_0 c_0 V_0 e^{i\frac{\omega}{c_0} - i\omega t} \tag{2.50}$$

$$v^* = V_0 e^{-i\frac{\omega}{c_0} + i\omega t} \tag{2.51}$$

When assuming plane waves in harmonic time domain, the sound power can thus be simplified as shown in equation (2.52).

$$N = \frac{1}{2}\mathrm{Re}\left[\frac{1}{T}\int_A \tilde{p}\tilde{v}^* dA\right] \tag{2.52}$$

The sound power can now be applied to determine the transmission loss in for instance an expansion chamber inserted between two smaller pipes with equal diameter. The reduction of the emitted sound can be determined by comparing the emitted sound power of the actual system against an idealised system, where the expansion chamber has the same dimensions as the connected pipes.

2.3.2 Transmission loss

The transmission loss of a transmission line is now considered by estimating the distribution of velocity potential in the system with application of the reduced wave equation for plane wave assumptions. The transmission line is modelled as three connected circular pipes with cross sectional area s_i where $i \in$ [1,2,3] and $s_1 = s_3$. The inlet pipe is connected to the expansion chamber at $x = L_1$ and the outlet is connected to the chamber at $x = L_1 + L_2$, see figure 2.1. It is assumed that both inlet and outlet has characteristic impedance boundary conditions or in other words, that the inlet and outlet pipes are infinitely long. Additionally it is assumed that reflective waves cannot interact with the source. On the inlet a pressure input of amplitude A_1 is applied at the frequency ω.

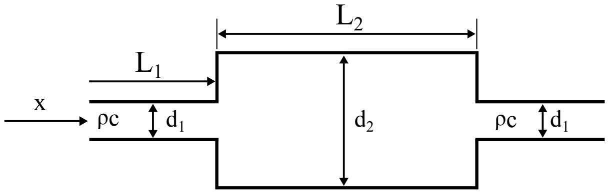

Figure 2.1: Sketch of the transmission line used for the analytical model.

To calculate the transmission loss, the distribution of velocity potential must first be determined throughout the system. In section 2.2.3 a solution to the homogeneous differential equation for the velocity potential was determined. The solution of the wave equation at each part of the transmission line is proposed as shown in equations (2.53), (2.54) and (2.55).

$$\varphi_1 = A_1 e^{ikx} + A_2 e^{-ikx} \tag{2.53}$$

$$\varphi_2 = A_3 e^{ikx} + A_4 e^{-ikx} \tag{2.54}$$

$$\varphi_3 = A_5 e^{ikx} \tag{2.55}$$

Where $k = \omega/c$ and A_1 is the amplitude of the input pressure which is taken as unity.

The pressure distribution in the tube is defined from equation (2.47) as $\widetilde{p}_i = i\rho\omega\varphi_i$. The volume velocity $q_i = \widetilde{v}_i s_i$ is introduced where $\widetilde{v}_i = \mathrm{d}\varphi_i/\mathrm{d}x$ and for a round pipe the cross sectional area $s_i = \pi d_i^2/4$. To ensure continuity in the system the following conditions must be satisfied at the transitions between different cross sectional areas.

$$\widetilde{p}_1|_{x=L_1} = \widetilde{p}_2|_{x=L_1} \tag{2.56}$$

$$\widetilde{p}_2|_{x=L_1+L_2} = \widetilde{p}_3|_{x=L_1+L_2} \tag{2.57}$$

$$\left.\frac{\partial\varphi_1}{\partial x}s_1\right|_{x=L_1} = \left.\frac{\partial\varphi_2}{\partial x}s_2\right|_{x=L_1} \tag{2.58}$$

$$\left.\frac{\partial\varphi_2}{\partial x}s_2\right|_{x=L_1+L_2} = \left.\frac{\partial\varphi_3}{\partial x}s_3\right|_{x=L_1+L_2} \tag{2.59}$$

As $i\rho\omega$ of the pressure distribution, is constant through the system, continuity in pressure is reduced to $\varphi_1 = \varphi_2$ at $x = L_1$. The following equations can be obtained from the continuity assumption where $s_1 = s_3$.

$$\varphi_1 = \varphi_2 \Rightarrow e^{ikL_1} + A_2 e^{-ikL_1} = A_3 e^{ikL_1} + A_4 e^{-ikL_1} \tag{2.60}$$

$$\frac{\mathrm{d}\varphi_1}{\mathrm{d}x}s_1 = \frac{\mathrm{d}\varphi_2}{\mathrm{d}x}s_2 \Rightarrow iks_1 e^{ikL_1} - iks_1 A_2 e^{-ikL_1} = iks_2 A_3 e^{ikL_1} - iks_2 A_4 e^{-ikL_1} \tag{2.61}$$

By isolating for A_2 in (2.60) and (2.61), and equating the, the following expression is determined.

$$A_2 = A_2 \quad \Rightarrow \quad A_3 e^{2ikL_1} + A_4 - e^{2ikL_1} = \frac{s_2}{s_1}A_4 - \frac{s_2}{s_1}A_3 e^{2ikL_1} + e^{2ikL_1} \tag{2.62}$$

Isolating for A_4 in (2.62) yields the equation below which only contains the unknown A_3.

$$A_4 = \frac{A_3\left(-\frac{s_2}{s_1}-1\right)e^{2ikL_1}+2e^{2ikL_1}}{\left(1-\frac{s_2}{s_1}\right)} \tag{2.63}$$

Applying continuity condition at $x = L_1 + L_2$ two expressions for A_5 and a new expression for A_4 can be determined.

$$A_5 = A_3 + \frac{A_3\left(-\frac{s_2}{s_1}-1\right)e^{2ik(L_1-L_2)}+2e^{ik(L_1-L_2)}}{\left(1-\frac{s_2}{s_1}\right)} \tag{2.64}$$

$$A_5 = \frac{s_2}{s_1}A_3 - \frac{s_2}{s_1}A_4 e^{-2ik(L_1+L_2)} \tag{2.65}$$

$$A_4 = \frac{1}{2}A_3\left(\frac{s_2}{s_1}-1\right)e^{2ik(L_1+L2)} \tag{2.66}$$

By setting (2.63) equal to (2.66) a final expression for A_3 is derived.

$$A_3 = \frac{2e^{2ikL_1}}{\left(\frac{s_2}{s_1}e^{2ik(L_1+L_2)}-\frac{1}{2}e^{2ik(L_1+L_2)}-\frac{1}{2}\frac{s_2^2}{s_1^2}e^{2ik(L_1+L_2)}+\frac{s_2}{s_1}e^{2ikL_1}+e^{2ikL_1}\right)} \tag{2.67}$$

To verify the analytical model the three tubes are assumed to have equal diameter, yielding the following results.

- If $s_1 = s_2 = s_3$ and $A_1 = 1$
- $A_1 = A_3 = A_5 = 1$
- $A_2 = A_4 = 0$

That $A_2 = A_4 = 0$ explains there are no reflection of the waves travelling through the system, which makes sense for a tube with uniform cross section. As the velocity potential is now established, the emitted sound power can be determined from the following expression, as explained in the previous section.

$$N_i = \frac{1}{2}\mathrm{Re}\left[\int_A \widetilde{p}_i\widetilde{v}_i^* dA\right] \tag{2.68}$$

By writing equation (2.68) it can be seen that the x dependency fades and emitted sound power stays constant throughout the system. The transmission loss (TL) is now determined by comparing the emitted sound power of the transmission line against the emitted sound power of the system with uniform cross section ($s_1 = s_2 = s_3$).

$$TL = 10\ log\left(\frac{N_{ideal}}{N_{reduced}}\right) \tag{2.69}$$

Where N_{ideal} is the sound power output of the idealised system with uniform cross section and $N_{reduced}$ is the sound power output of the transmission line.

The analytical model derived in this section, is applied in the ensuing chapter to compare the transmission loss against a finite element model of the actual muffler design.

Development of numerical model 3

Now that the common terminology used in acoustics are explained and familiar, an numerical acoustic model can be developed. An numerical model is preferable to an analytical model as it can account for effects and disturbances (geometric changes etc.) a simple analytical model cannot when using linear theory of acoustics without overcomplicating the equations. The purpose of this chapter is to present an initial FE model aiming to study the suitable element technology, as well as the effect of the element size in the accuracy of the acoustic analysis.

3.1 Validation of the initial finite element model

The first step in order to build an numerical model is to compare an analytical model with an numerical model using simplified geometry and boundary conditions with the purpose to test the element technology and the mesh size suitable for the FE model. Short calculation time is desired, so implementation of a reasonably large mesh while still acquiring reliable results are of importance. Aiming to test the mesh quality, the acoustic field of a cylindrical-shaped region enclosed by rigid walls is considered. The analytical solution of the modal analysis in the mentioned case is well known, therefore the quality of the mesh used in the FE model can be easily tested by comparison of the FE modal analysis, where the analytical solution is assumed to be exact. In the following section the analytical modal analysis is presented firstly, afterwards the equivalent FE modal analysis is described and comparison of the results are discussed.

3.1.1 Analytical modal analysis

To verify the FE model a basic acoustic model is developed from the dimensions provided from *Lloyd's Register* and the acoustic domain is assumed to have fixed boundaries, seen on figure 3.1. The acoustic medium is air, and it is assumed to have a constant density of $\rho = 1.225\,[\mathrm{Kg/m^3}]$.

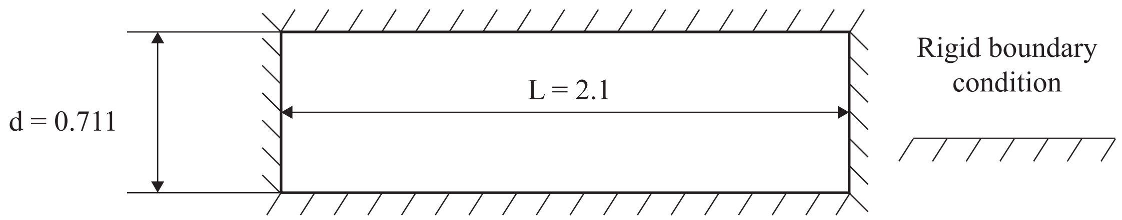

Figure 3.1: Dimensions and boundary conditions of the cylindrical acoustic field analysed. Dimensions expressed in [m].

When the sound is propagating inside a cylindrical rigid boundary, the sound is forced to travel parallel to the length axis. This is called a *wave guide*. Under the assumptions of straight tube, infinite length and uniform circular cross-section, Helmholtz equation is written as:

$$\frac{\partial^2 \widetilde{\varphi}}{\partial r^2} + \frac{1}{r}\frac{\partial \widetilde{\varphi}}{\partial r} + \frac{1}{r^2}\frac{\partial^2 \widetilde{\varphi}}{\partial \theta^2} + \frac{\partial^2 \widetilde{\varphi}}{\partial x^2} + \frac{\omega^2}{c^2}\widetilde{\varphi} = 0 \tag{3.1}$$

And the rigid wall boundary conditions:

$$\left.\frac{\partial \widetilde{\varphi}}{\partial r}\right|_{r=r_0} = 0 \quad ; \quad \left.\frac{\partial \widetilde{\varphi}}{\partial x}\right|_{x=0} = 0 \quad ; \quad \left.\frac{\partial \widetilde{\varphi}}{\partial x}\right|_{x=L} = 0 \tag{3.2}$$

Equation (3.1) has a trivial solution where $\widetilde{\varphi} = 0$. However, equation (3.1) has infinitely many non-trivial solutions. These non-trivial solution are the eigenmodes of the free vibration. The eigenmodes are determined by using equation (3.3) as a guess for $\widetilde{\varphi}$ in equation (3.1) which satisfy every boundary condition:

$$\widetilde{\varphi}(r,\theta,x) = \sum_{m=0}^{\infty}\sum_{n=0}^{\infty} \widetilde{\varphi}(r)_{mn} cos(m\theta) cos\left(\frac{n\pi x}{L}\right) \tag{3.3}$$

In equation (3.3) first factor of the product express the velocity potential dependency on the radius of the cavity. The second factor depends on the so-called circumferential wave number m, which represents the harmonic behaviour of the wave at each cross section of the duct. Finally, the third factor in equation (3.3), which is x dependent, accounts for the harmonic behaviour along the length of the cavity where $n = 1,2,\ldots\infty$.

The partial differential terms in equation (3.1) is shown in equation (3.4).

$$
\begin{aligned}
\frac{\partial \widetilde{\varphi}}{\partial r} &= \frac{\partial \widetilde{\varphi}(r)_{mn}}{\partial r} cos(m\theta) cos\left(\frac{n\pi x}{L}\right) \\
\frac{\partial^2 \widetilde{\varphi}}{\partial r^2} &= \frac{\partial^2 \widetilde{\varphi}(r)_{mn}}{\partial r^2} cos(m\theta) cos\left(\frac{n\pi x}{L}\right) \\
\frac{\partial^2 \widetilde{\varphi}}{\partial \theta^2} &= -m^2 \widetilde{\varphi}(r)_{mn} cos(m\theta) cos\left(\frac{n\pi x}{L}\right) \\
\frac{\partial^2 \widetilde{\varphi}}{\partial x^2} &= -\left(\frac{n\pi}{L}\right)^2 \widetilde{\varphi}(r)_{mn} cos(m\theta) cos\left(\frac{n\pi x}{L}\right)
\end{aligned}
\tag{3.4}
$$

The solution of the wave equation must be harmonic along the axial coordinate x. The term $cos(\frac{n\pi x}{L})$ in equation (3.4) is simplified to $cos(kx)$, thereby $k = \frac{n\pi}{L}$. The derivatives shown in equation (3.4) and $k = \frac{n\pi}{L}$ are substituted into equation (3.1), and the term $cos(m\theta)cos(kx)$ is factored out, yielding equation (3.5).

$$
\frac{\partial^2 \widetilde{\varphi}_{mn}(r)}{\partial r^2} + \frac{1}{r}\frac{\partial \widetilde{\varphi}_{mn}}{\partial r} - \frac{1}{r^2} m^2 \widetilde{\varphi}_{mn}(r) - k^2 \widetilde{\varphi}_{mn}(r) + \frac{\omega^2}{c^2} \widetilde{\varphi}_{mn}(r) = 0 \tag{3.5}
$$

The expression is rearranged to:

$$
\frac{\partial^2 \widetilde{\varphi}_{mn}(r)}{\partial r^2} + \frac{1}{r}\frac{\partial \widetilde{\varphi}_{mn}}{\partial r} - \frac{1}{r^2} m^2 \widetilde{\varphi}_{mn}(r) + \left(\frac{\omega^2}{c^2} - k^2\right) \widetilde{\varphi}_{mn}(r) = 0 \tag{3.6}
$$

Equation (3.6) is recognized to have a solution in the form of a Bessel function. The Bessel function consists of two kinds. The Bessel equations of the first kind and second kind can be seen on figure 3.2 and figure 3.3 respectively.

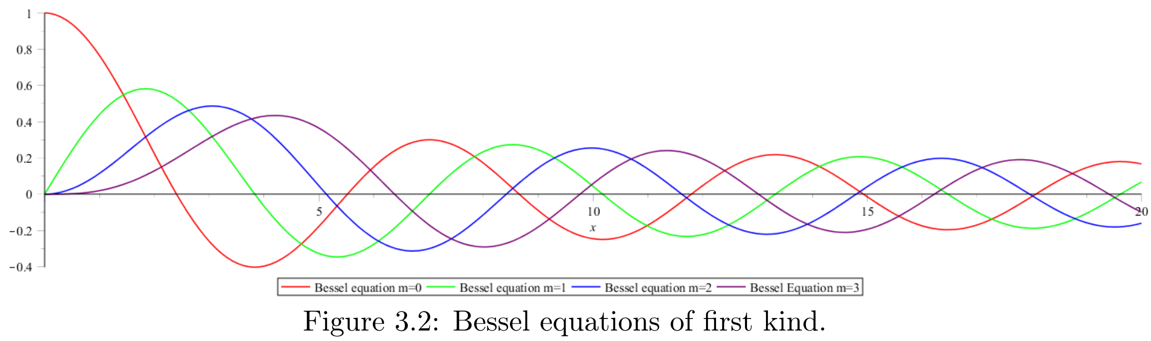

Figure 3.2: Bessel equations of first kind.

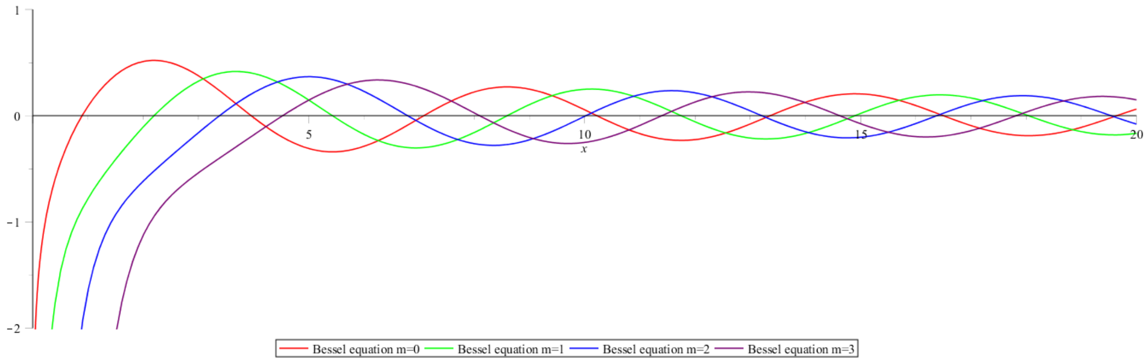

Figure 3.3: Bessel equations of second kind.

The Bessel equations are defined in a dimensionless domain, so in order to express equation (3.6) in dimensionless domain, a radius relation $\bar{r}$ is introduced as the ratio of any radial distance r over the total radius r_0, see figure 3.4.

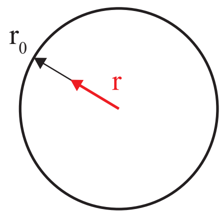

Figure 3.4: Graphical representation of the radius relation.

The radius relation is introduced in equation (3.6) as $r = \bar{r}\, r_0$, so that it becomes:

$$\frac{1}{r_0^2}\frac{d^2\widetilde{\varphi}_{mn}(r)}{d\bar{r}^2} + \frac{1}{r_0\,\bar{r}}\frac{1}{r_0}\frac{d\widetilde{\varphi}_{mn}}{d\bar{r}} - \frac{1}{(r_0\,\bar{r})^2}m^2\widetilde{\varphi}_{mn}(r) + \left(\frac{\omega^2}{c^2} - k^2\right)\widetilde{\varphi}_{mn}(r) = 0 \tag{3.7}$$

Equation (3.7) is further simplified by multiplying with r_0^2:

$$\frac{d^2\widetilde{\varphi}_{mn}(r)}{d\bar{r}^2} + \frac{1}{\bar{r}}\frac{d\widetilde{\varphi}_{mn}}{d\bar{r}} - \frac{1}{\bar{r}^2}m^2\widetilde{\varphi}_{mn}(r) + \left(\frac{\omega^2}{c^2}r_0^2 - k^2 r_0^2\right)\widetilde{\varphi}_{mn}(r) = 0 \tag{3.8}$$

Equation (3.8) is a Bessel equation and its general mentioned in equation (3.9).

$$\widetilde{\varphi}_{mn}(\bar{r}) = A_m J_m(\kappa\bar{r}) + B_m Y_m(\kappa\bar{r}) \tag{3.9}$$

Where J_m and Y_m are the Bessel functions of first and second kind respectively and $\kappa\bar{r}$ is the argument of the Bessel functions where κ is given by equation (3.10).

$$\kappa = \sqrt{\frac{w^2}{c^2} - k^2} \tag{3.10}$$

The acoustic pressure and velocity potential are bounded at $r = 0$ and taking into account that the Bessel function of second kind Y_m tends to infinity as r approaches 0, see figure 3.3, the constant B_m is set to zero. Then the rigid wall boundary condition is applied as:

$$\left.\frac{d\,\widetilde{\varphi}_{mn}(\bar{r})}{d\bar{r}}\right|_{\bar{r}=1} = 0 \quad \rightarrow \quad A_m\left.\frac{d\,J_m(\kappa\bar{r})}{d\bar{r}}\right|_{\bar{r}=1} = 0 \tag{3.11}$$

The set of non-trivial solutions is given by $A_m \neq 0$, then:

$$\left.\frac{d\,J_m(\kappa\bar{r})}{d\bar{r}}\right|_{\bar{r}=1} = 0 \tag{3.12}$$

Equation (3.12) is known as a dispersion equation and it provides a relation between the excitation frequency w, the circumferential wave number m and the wave number k of a propagating wave. The condition (3.12) allows to estimate the pressure and velocity distributions in the acoustic field once the excitation frequency w is found. The acoustic pressure distribution is analogous to the eigenmode of mechanical vibration while the excitation frequency is analogous to the eigenfrequency. In order to estimate the eigenfrequencies, let us consider the graphical representation of the derivative of the Bessel function, equation (3.12) where $m = 0$, represented in figure 3.5.

$$\left.\frac{d\,J_0(\kappa\bar{r})}{d\bar{r}}\right|_{\bar{r}=1} = \kappa J_1(\kappa\bar{r}) = 0 \tag{3.13}$$

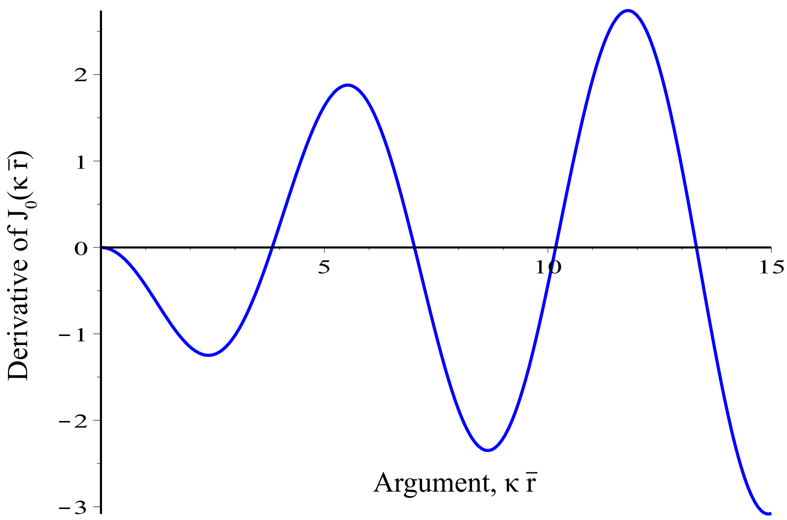

Figure 3.5: Graphical representation of the derivative of the Bessel function $J_0(\kappa\bar{r})$.

The condition given in equation (3.12) is represented in figure 3.5 by the locations where the curve cuts the 0 ordinate axis. The first zero of the the Bessel function derivative fulfilling the condition (3.12), corresponds to an argument $\kappa_1\bar{r}|_{\bar{r}=1} = \sqrt{\frac{w_n^2}{c^2} - k_n^2} = 0$ which provides infinitely many roots since $k_n = \frac{n\pi}{L}$ contains the integer $n = 1,2\ldots\infty$. From this it is obvious the relation $k_n = \frac{w_n}{c}$ which is only valid for the circumferential wave number $m = 0$ since the derivative of J_0 is the only one which has a root at the argument $\kappa_1\bar{r}|_{\bar{r}=1} = 0$. The eigenfrequencies are found by isolating w in the expressions of the arguments at the points where the derivative of the Bessel function is zero. Taking into account that infinitely many eigenfrequencies are obtained for each zero of the Bessel function derivative, an upper bound of 2000 [Hz] is established in order to find the eigenfrequencies.

Once the eigenfrequencies are determined, it is important to know the mode shapes of each frequencyas it is essential to know the mode shape in order to compare frequencies between models. In the FE model presented in the next section, the mode shape is given by the acoustic pressure distribution whereas the analytical mode shape is obtained by means of the velocity potential distribution given by equation (3.3). As it is already known that the velocity potential varies in the radial direction according to the Bessel function of first kind J_m, equation (3.3) is rewritten as:

$$\widetilde{\varphi}(r,\theta,x) = \sum_{m=0}^{\infty}\sum_{n=0}^{\infty} J_m(\kappa\bar{r})cos(m\theta)cos\left(\frac{n\pi x}{L}\right) \tag{3.14}$$

Since the purpose is to look at the pressure distribution at the outer surface of the acoustic field, the amplitude of the velocity potential is equal to 1, therefore $J_m(\kappa\bar{r}) = 1$. The mode shape is finally obtained by making a 3-D plot of equation (3.14) with $\theta \in [0,2\pi]$ and $x \in [0,L]$. For instance, the circumferential wave number $m = 1$ and the longitudinal wave number $n = 1$, provide the velocity potential distribution shown in figure 3.6, which should represent the shape of the pressure distribution provided by the numerical model in ANSYS®.

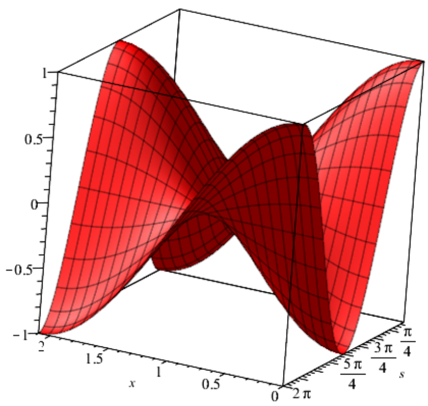

Figure 3.6: 3-D plot of the mode shape analytical prediction corresponding to $m = 1$ and $n = 1$.

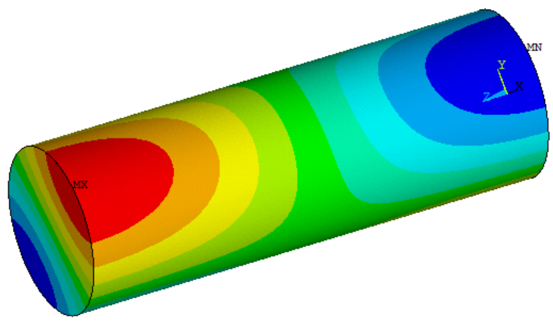

Figure 3.7: Plot of the mode shape of an FE model corresponding to $m = 1$ and $n = 1$.

Note that the 3-D plot in figure 3.6 corresponds to the unfolded cylindrical acoustic field, therefore the domain is given as a rectangle with the following dimensions: 1) The depth $\theta \in [0,2\pi]$ representing the circumferential direction. 2) The width $x \in [0,L]$ representing the longitudinal direction. Comparing figure 3.6 and figure 3.7 it is noted that the mode shapes are indeed equal, and the models are comparable.

At this point it is convenient to introduce the concept of cut-on frequency which is obtained when the wave number $k = 0$, meaning that $n = 0$. Below the cut-on frequency the wave number k is not a real number, therefore according to the emitted sound power (2.49) these waves do not convey energy. For $m = 0$ which is denoted as duct mode, all the frequencies carry energy since its cut-on frequency is $w = 0$, whereas for different circumferential wave numbers the cut-on frequency is greater than zero, therefore not all the frequencies convey energy. The waves travelling at frequencies below the cut-on frequencies are called evanescent waves and they are not relevant in the analysis of noise transmission since they do not produce work and therefore, no sound is created. A select few cut-on frequencies for the simple geometry can be seen in table 3.1.

Cut-on frequencies				
n/m	**0**	**1**	**2**	**3**
1	0	282.55	468.97	645.1
2	588.15	818.68	1029.76	1230.77
3	1077.36	1310.78	1530.82	1742.28

Table 3.1: A selected number of cut-on frequencies. The full table can be found in the appendix.

Håvard Borvik Kleppe Note!

[1] This section has dealt with the analytical estimation of the eigenfrequencies of a simple acoustic model in order to validate the element size of the equivalent FE analysis which is presented in the next section.

3.1.2 FE modal analysis

The geometry of the FE modal analysis is a 3-D cylinder where all the walls are assumed to be rigid. When carrying out an acoustic analysis in ANSYS®, the so-called FLUID elements are used. This analysis aims to test the acoustic 3-D elements FLUID 220, FLUID 221 and FLUID 30 with the purpose of selecting a determined element technology for posterior FE analyses. As mentioned, this task is accomplished by comparison of the eigenfrequencies obtained from the FE modal analysis with the eigenfrequencies obtained from the anlytical modal analysis. The element technology is shown in table 3.2 and the analysis characteristics are described in table 3.3. Both hexahedral and tetrahedral can be seen on figure 3.8 and figure 3.9 respectively.

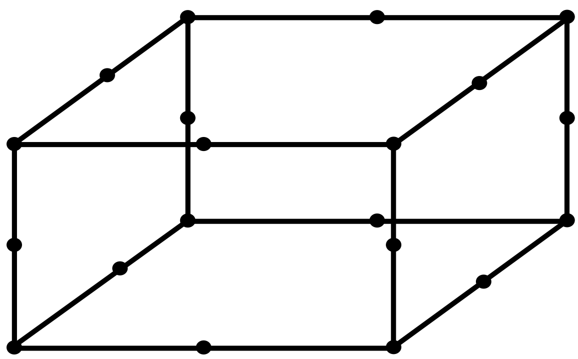

Figure 3.8: Sketch of a hexahedral element.

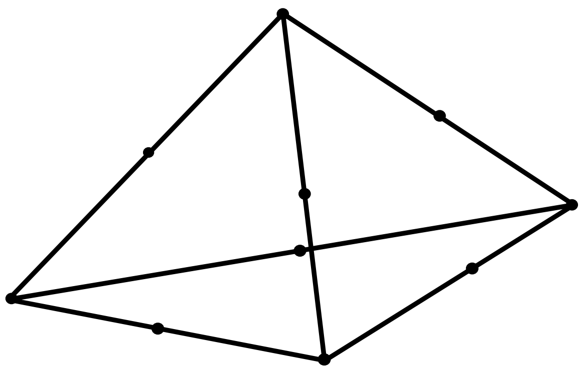

Figure 3.9: Sketch of a tetrahedral element.

[1] Håvard Borvik
Kleppe Note: remember to say which appendix when it has been added

Element technology				
Name	**Order**	**Shape**	**Nodes**	**Element matrix**
FLUID 220	quadratic	hexahedral	20	symmetric
FLUID 221	quadratic	tetrahedral	10	symmetric
FLUID 30	linear	hexahedral	8	symmetric

Table 3.2: Different acoustic elements tested.

Characteristics of modal analysis	
Geometry	Cylindrical region according to the dimensions shown in figure 3.1
Boundary conditions	All the walls are assumed to be rigid as represented in figure 3.1. If no boundary condition is specified, ANSYS®assumes all the model boundaries as rigid
Structural influence	The interaction with the structure is not taken into account, therefore according to the manual, symmetric element matrix is chosen in the element key options.
Element size	An element size of 5 [cm] is specified.
Load	Excitation is not considered as it is a modal analysis
Solver	The analysis type is set as modal analysis and the method chosen for extracting the eigenfrequencies is the Block Lanczos method since it is suitable for symmetric element matrices, [Theory Reference, 2013]. Eigenfrequencies are calculated up to 2000 [Hz].

Table 3.3: Characteristics of the FE modal analysis of the cylindrical acoustic field.

From the analytical modal analysis it is known that there are infinitely many eigenfrequencies for single values of the circumferential wave number m and the longitudinal wave number n. It has been said before that in order to compare analytical and numerical models, the frequencies analysed must create the same mode shape so they are comparable. Continuing, the frequencies obtained from the analytical model 294.11 Hz, 822.74 Hz, 1313.32 Hz and 1799.41 Hz which corresponds to the mode $m = 1$ and $n = 1$ are considered. For each element technology, the error in the estimation of the eigenfrequencies, the solution time and the number of elements contained in the model are compared. The differences regarding solution time and discretization are shown in table 3.4.

Name	Solution time [s]	Number of elements
FLUID 220	121	12600
FLUID 221	219	65968
FLUID 30	21	12600

Table 3.4: Performance of the acoustic elements regarding solution time and number of elements forming the model.

It is visible in table 3.4 that the solution provided by FLUID 30 is very fast compared to the solution time offered by quadratic elements, the consequence of this is obviously that the linear element has less number of nodes than the quadratic acoustic elements. Note that although the number of nodes of the element FLUID 221 (10 nodes) is less than the number of nodes of the element FLUID 220 (20 nodes), the solution takes longer when the analysis is executed with FLUID 221. This issue is due to the large amount of elements FLUID 221 which are generated in the model for an established element size of 5 cm (65968 FLUID 221 elements compared to 12600 elements created in case of using FLUID 220). The element size specifies the approximate length of the element edges. Thus, it must be considered that even though the element size is established as 5 cm in all the models, FLUID 221 is a tetrahedral element, therefore it has less number of faces than FLUID 220 or FLUID 30 which are hexahedral elements. Having less number of faces, it is possible to fit a larger amount of tetrahedral elements than hexahedral elements in the same volume for the same element size.

The error in the estimation of the eigenfrequencies generating the mode shape $m = 1$, $n = 1$ is considered in table 3.5 where the disagreement with respect to the analytical solution is expressed in relative error.

Analytical result [Hz]	**Element Type**	**FE result [Hz]**	**Error [%]**
294.11	FLUID 220	294.29	0.061
	FLUID 221	294.29	0.061
	FLUID 30	294.95	0.286
822.74	FLUID 220	822.81	0.009
	FLUID 221	822.85	0.013
	FLUID 30	834.38	1.415
1313.32	FLUID 220	1314.12	0.061
	FLUID 221	1314.41	0.083
	FLUID 30	1372.67	4.519
1799.41	FLUID 220	1803.12	0.206
	FLUID 221	1804.34	0.274
	FLUID 30	not found	-

Table 3.5: Relative error of the numerical solution provided by different acoustic elements with respect to the analytical solution.

By looking at table 3.5 it is very obvious that the results deviate from the analytical solution. As the frequency increases the number of elements needs to increase to capture a full wave. If your mesh is too small the full wave behaviour cannot be determined as the wave length is smaller. It is also visible that the performance of the linear element is very poor compared to quadratic elements. The accuracy of quadratic elements is a consequence of their midside node. The presence of the midside node eases the description of the wave behaviour when the wave length is rather small. Finally it is worth to noting that the accuracy of the analyses carried out with FLUID 220 is slightly better than the accuracy of the model meshed with FLUID 221, despite the finer mesh presented by the last. Hence it is demonstrated that the acoustic element FLUID 220 provides a good performance with rather coarse mesh, probably due to its 20 nodes. FLUID 221 which is a 10 nodes element needs a finer mesh in order to accomplish results of the same level of accuracy than FLUID 220.

Even though FLUID 220 has demonstrated to behave better than FLUID 221, in future models the priority is to mesh with acoustic elements FLUID 221 because they have also shown to be accurate with respect to the analytical solution and most importantly, it is easier to create the mesh with tetrahedral elements when a model exhibits certain degree of complexity in geometry.

As it is commented on in the beginning of this chapter, the second reason of comparing analytical and numerical modal analysis is to test the mesh size. It is very common in acoustics to define the element size depending on the wave length. A rule of thumb is that 5 elements per wave length (in the case of quadratic elements) are required to describe the acoustic behaviour properly. The analysis that has been presented in this section, sets an upper bound of 2000 [HZ] in order to narrow down the range of relevant eigenfrequencies, therefore 2000 [Hz] is the frequency with the shortest wave length, meaning that it provides the finest mesh according to the rule of thumb. The wave length is given by $\lambda = c/f$ where $c = 343$ [m/s] and $f = 2000$[Hz], thus $\lambda = 0.171$[m]. Remember that the element size used in the analysis which is presented above is 0.05 [m] and this yields a mesh containing approximately 3 elements per wave length. It turns out that the mesh used is coarser than the mesh recommended. However, the analysis has demonstrated good agreement with the analytical solution even for high frequencies (0.274% was the highest error obtained). This consideration allows to establish an element size of $\lambda/3$ as the coarser mesh rule for subsequent models. Even though the results obtained show that coarser meshes could be used, it must be considered that the model where the mesh has been tested is very simple and the accuracy might be reduced in more complex models. Hence as a conservative consideration, in subsequent models the mesh size is finer or equal than the one provided by the rule $\lambda/5$.

3.2 Transmission loss in the muffler

After the suitable element technology and mesh requirements are considered in the previous section, this section is aimed to build a FE model of the muffler which allows to see how much energy is naturally lost when the air travels through the muffler i.e. a reflective muffler. The analysis of a pure reflective muffler is interesting because it provides an idea of how the sound is attenuated only due to the geometry of the expansion chamber before any absorbing solution is introduced. In order to construct this model, the transmission loss is determined analytically for a model with simplified geometry. This simplified analytical model is the reference for validating the performance of an equivalent FE model with the same simplified geometry. Once the simplified FE model is validated, the real geometry is introduced in the model so that it is possible to obtain the transmission loss in the real reflective muffler.

3.2.1 Analytical transmission loss

The analytical model (figure 3.10) is modelled with a standard cylindrical expansion chamber using planar wave theory. At the end of both the inlet and outlet there is a ρc boundary condition to represent free flow through the pipes. The boundary condition on the inlet also prevents disturbance from reflecting waves on the input source. This represents an assumption that the input source has a constant amplitude during excitation at a certain frequency. In this case the input source is applied as a normal velocity which oscillates with unit amplitude within the range of frequencies [0,1000] Hz.

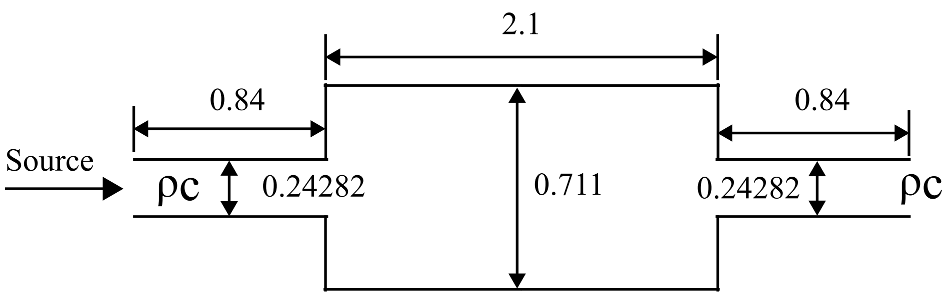

Figure 3.10: Sketch of the analytical model for calculating the transmission loss.

Following the approach presented in section 2.3.2 *Transmission loss*, the transmission loss is calculated for the range of frequencies [0,1000] Hz and represented in figure 3.11. Note that the range of frequencies in figure 3.11 is expressed in $\frac{1}{s}$.

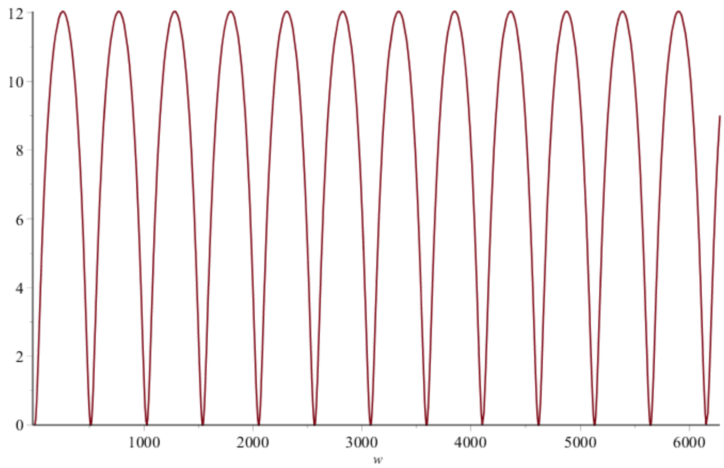

Figure 3.11: Transmission loss dB - angular velocity $\frac{1}{s}$ diagram.

Figure 3.11 shows a continuous oscillation of the transmission loss. It is important to note that the analytical model only considers plane waves travelling through the system, however in reality, mixed modes might influence the transmission loss after a certain frequency. By investigation of the wave length, where $\lambda = \frac{c}{f[Hz]}$, it can be seen that peaks in transmission loss occurs when the wave ends in a quarter wave in the muffler. This will lead to largest reflecting wave. At the pits of the curve the waves are a half oscillation when it exits the muffler leading to no reflection of the waves, illustrated on figure 3.12

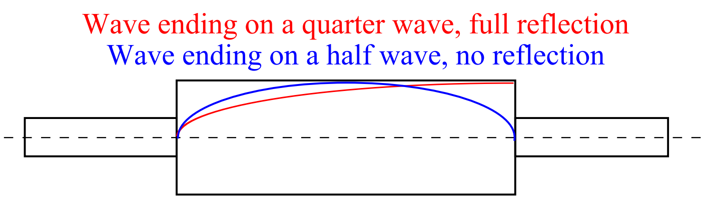

Figure 3.12: Illustration of low frequencies ending at certain wave lengths in the muffler.

Now that the transmission loss has been defined analytically, let us solve the same example by using finite element methods in order to check if the FE model predicts the transmission loss accurately.

3.2.2 Finite Element Model

To make sure the finite element model for transmission loss is reliable, a simple model resembling the model used for the analytical model is developed. The finite element model is conducted using the 10 node element FLUID 221 where the mesh size is determined by the wave length of the frequency i.e. $\lambda_{freq}/7$. The element size represented in figure 3.13 is decided from the element study described in section 3.1.2 *FE modal analysis*. This will reduce the calculation time while making sure there are a sufficient amount of elements per frequency. The plane input is modelled in ANSYS® by specifying a normal velocity of the nodes at the inlet surface. [2] As pressure is usually applied as input the normal velocity is determined from equation (3.15) by choosing a pressure input.

Rasmus Julsgaard Note!

$$v_n = \frac{p_i}{\rho \cdot c_0} \tag{3.15}$$

Where v_n is the normal velocity on the inlet and p_i the desired pressure input which is set to unity in the following analysis.

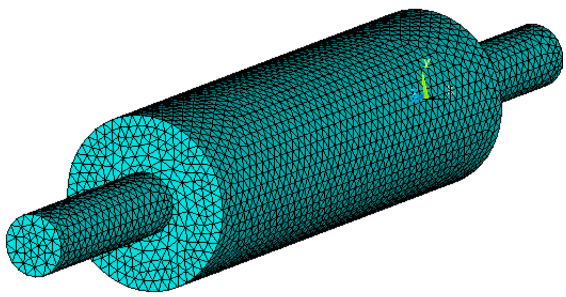

Figure 3.13: Finite element model of a simple transmission loss analysis.

The initial analysis was performed only using a ρc boundary condition at the outlet. This resulted in inconsistent oscillation throughout the entire frequency range, shown on figure 3.14.

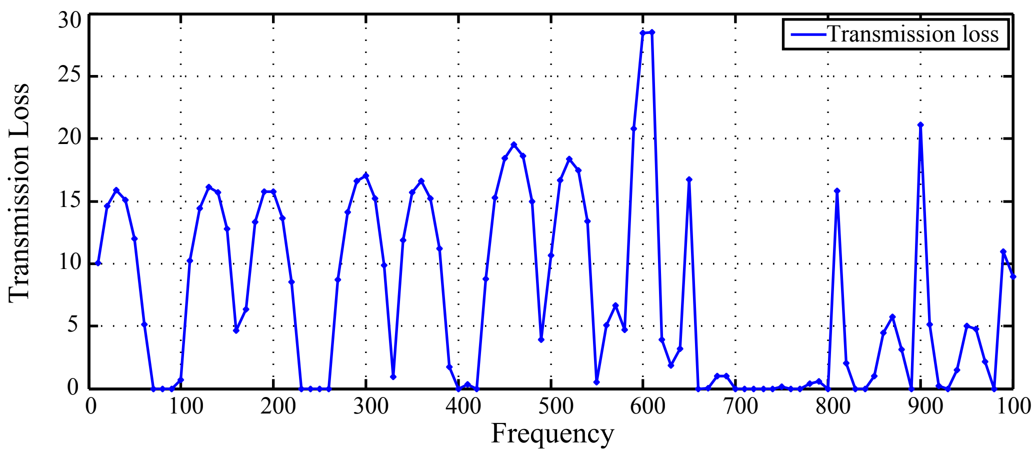

Figure 3.14: Transmission loss dB - Frequency Hz for impedance boundary condition on the outlet.

[2] Rasmus
Julsgaard Note: make a figure showing this

It can be seen that figure 3.14 only follows figure 3.11 for the first oscillation. It can be noted that the pits where $TL = 0$ continues for a larger range of frequencies in the FE model compared the analytical model. By applying a ρc boundary condition on the inlet the transmission loss curve tends to follow figure 3.11 until the first cut-off frequency is reached, see figure 3.15.

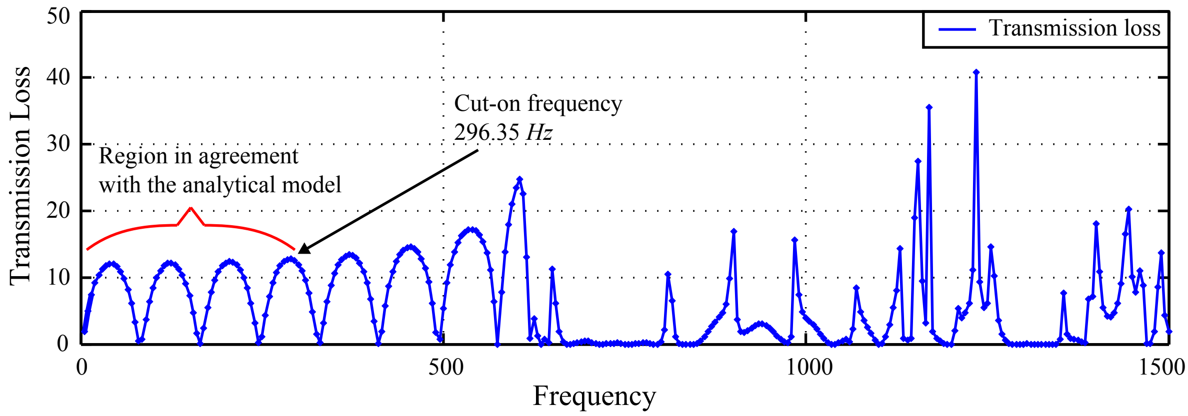

Figure 3.15: Transmission loss dB - Frequency Hz for impedance boundary condition on the inlet and outlet.

This indicates that the input source is influenced by the reflecting waves on the first FE model, which means that the FE model does not comply with the assumption made in the analytical model which dictates that the reflected waves does not influence the source. Note that figure 3.15 is consistent with figure 3.11 until the first cut-on frequency $296.35 Hz$, which corresponds to $m = 1$, see figure 3.16. It is known that the mode shape shown in figure 3.16 is a cut-on frequency because the pressure distribution is constant along the length, meaning that the longitudinal wave number, $n = 0$. The discrepancy after the first cut-on frequency is because the analytical model only considers plane waves, where the FE model includes every mode affecting the frequencies. However as analytical and FE model are in good agreement inside the plane wave range, it can be said that the FE model is valid.

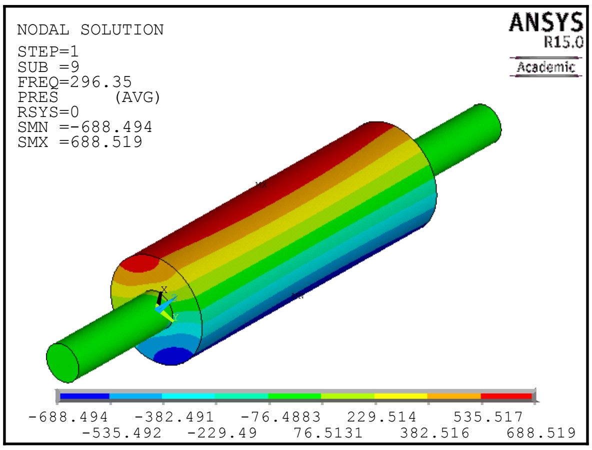

Figure 3.16: Pressure distribution of the first cut-on frequency in the simplified model.

Now that the FE model with simplified geometry is verified by comparison with the equivalent analytical model, the realistic model can be implemented into ANSYS®. This real model is built according to the geometry shown in figure 1.1 and the mesh size is the same than the one used in the case of simplified geometry, see figure 3.17.

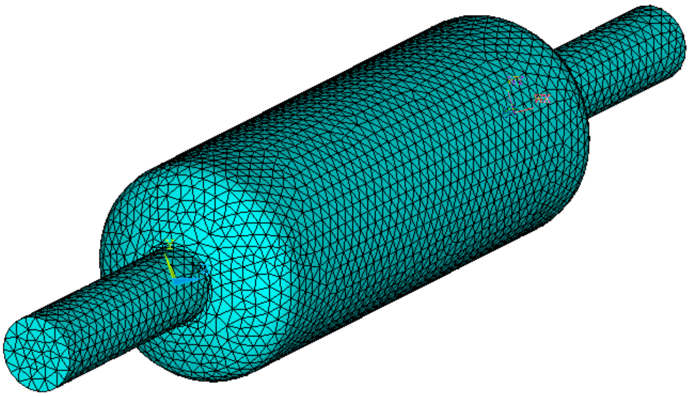

Figure 3.17: Finite Element model of the realistic system.

A graph showing the change in transmission loss with respect to frequency can be seen on figure 3.18.

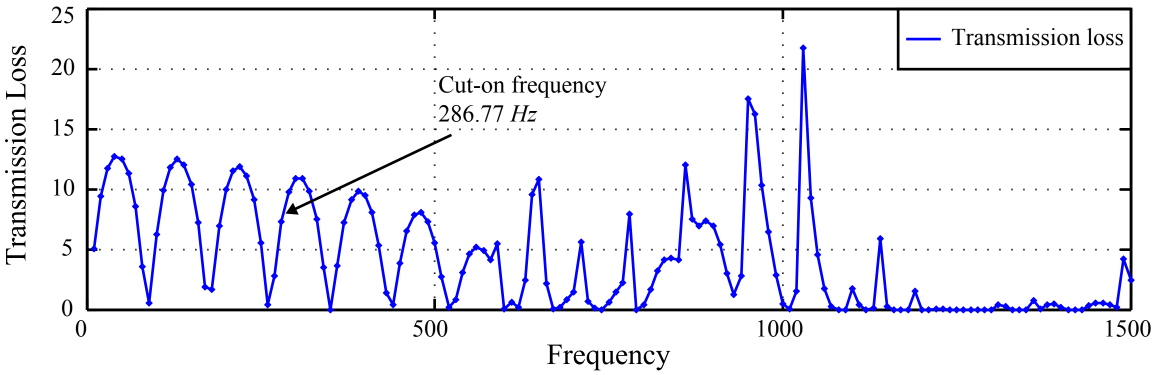

Figure 3.18: Transmission loss dB - Frequency Hz graph for finite element model of realistic model using two ρc boundary conditions.

Comparing figure 3.15 with figure 3.18 it can be seen that the transmission loss of the realistic model tends to have a decrease of transmission loss slightly before it reaches its first cut-on frequency where the simple model has an increase in transmission loss. Intuitively this seems to be a consequence of the curved edges contained in the real model.

Through the outline of this chapter have, a pure reflective muffler has been modelled by using finite element methods. Once such a model has been validated, it is used in the next section in order to examine the pressure distributions inside the muffler.

3.3 Examination of eigen modes at driving frequencies

In the previous section, a pure reflective version of the muffler has been modelled. While working in the validation of the FE reflective muffler, it was observed that the FE model with simplified geometry (no curved edges) only showed plane modes when the model was excited in order to obtain the transmission loss. On the other hand it was found that the FE model with real geometry displayed mixed modes for some frequencies. Thus the purpose of this section is to investigate why mixed modes are present in the real model and check if these also appear at the driving frequencies specified by *Lloyd's Register*. It is worth to emphasise that the fact of not having mixed modes (only plane waves) at the driving frequencies is beneficial since it introduces the possibility of applying simplifications if needed. These potential simplifications would be based on the axisymmetric pressure distributions generated by plane waves.

Let us consider the eigen mode displayed by the FE model with simplified geometry corresponding to the eigen frequency 888.61 Hz in figure 3.19a. It is visible that this eigen mode corresponds to $m = 4$ and $n = 2$. However when the response of the systems is examined in the vicinity of this frequency, at 888.50 Hz, no sign of the eigenmode appears, see figure 3.19b. Note that the input is a plane wave and thus shows no mixed modes because of the concentric and axissymmetric nature of the model.

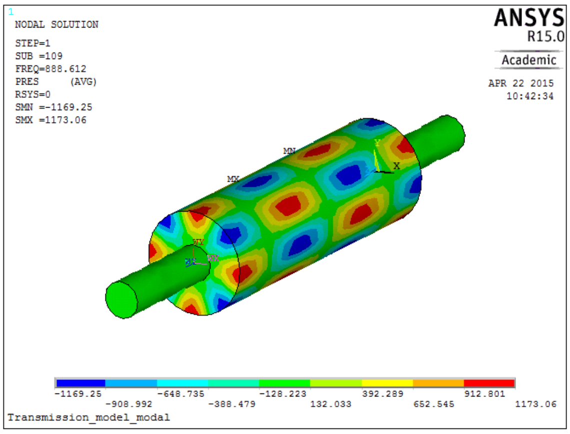

(a) Modal analysis of initial FE-model. Mode shape corresponding to $m = 4$ and $n = 2$ at 888.61 Hz.

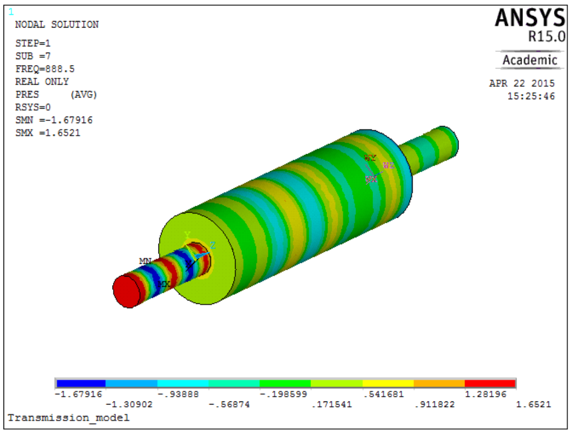

(b) Harmonic analysis of initial FE-model with plane input at 888.50 Hz only displaying longitudinal modes.

Figure 3.19: Comparison between eigenmodes and response of initial model using plane input.

Rasmus Julsgaard Note!

3

The result is rather different when the detailed model is considered. When the ends of the muffler are curved instead of flat, they allow for some dispersion of the waves leading to the results seen in figures 3.20a and 3.20b.

[3]Rasmus
Julsgaard Note: might need reformulation

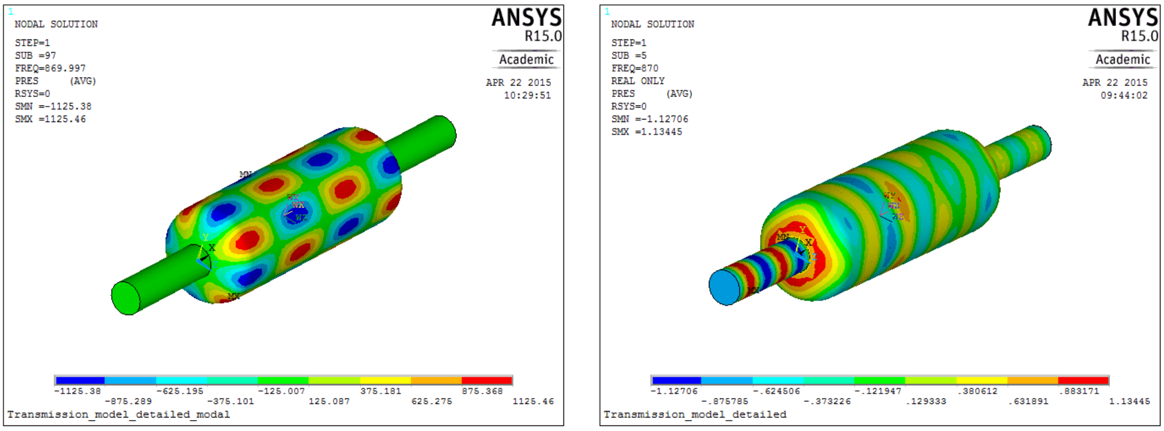

(a) Modal analysis of detailed FE-model. Mode shape corresponding to $m = 4$ and $n = 2$ at 869.99 Hz.

(b) Harmonic analysis of detailed FE-model with plane input at 870.00 Hz displaying a pressure distribution similar to the eigen mode.

Figure 3.20: Comparison between eigenmodes and response of detailed model using plane input.

The mixed modes are excited in the harmonic response analysis of the detailed model, although some interference is observed. This means that, contrary to the initial model, if a mixed eigenmode is excited it will be visible in the response of the system and thus not allow for 2D simplification of the system. Consequently it is important to check that the driving frequencies of the muffler are not close to any eigenfrequency.

Consider the driving frequencies provided by Lloyd's Register which are shown in table 3.6. This frequencies are applied to the FE model with real geometry in order check whether mixed modes will be present in the response.

Driving frequencies		
Fundamental frequency	**2^{nd} harmonic**	**3^{rd} harmonic**
446 Hz	892 Hz	1338 Hz

Table 3.6: Driving frequency with 1^{st}, 2^{nd} and 3^{rd} harmonics.

Once the driving frequencies are applied to the detailed FE model of the muffler, the obtained pressure distributions are shown in figure 3.21

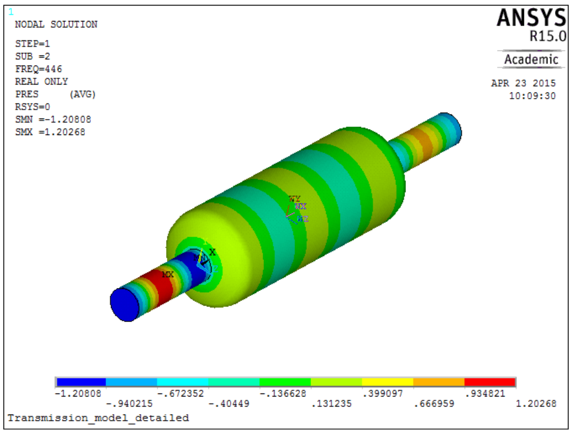

(a) Response of detailed model at the driving frequency of 446 Hz with plane input.

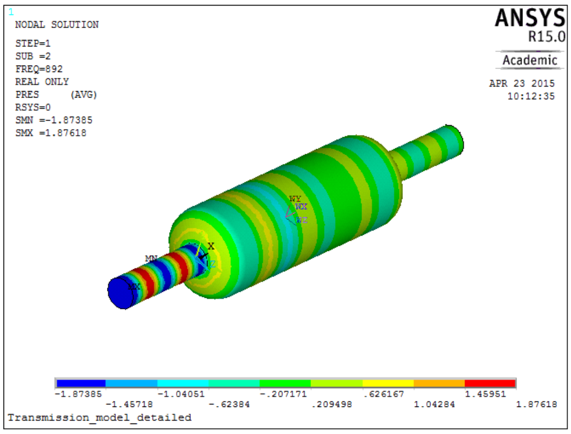

(b) Response of detailed model at the 2^{nd} harmonic (892 Hz) with plane input.

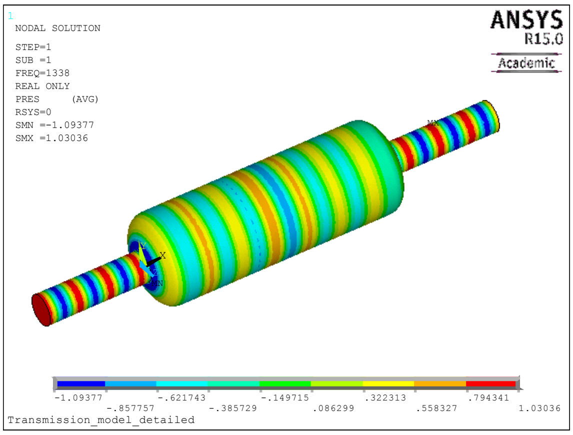

(c) Response of detailed model at the 3^{rd} harmonic (1338 Hz) with plane input.

Figure 3.21: Pressure distributions generated in the detailed model when it is excited by the driving frequencies.

Since the pressure distribution observed in figure 3.21 are axisymmetric, it is proved that there are not mixed mode when the driving frequencies are applied. In conclusion, simplifications of the model might be used, based on the fact that axisymmetric pressure distributions are generated by the driving frequencies.

Remember that the FE model of the muffler presented so far is pure reflective. In the next section a dissipative solution is considered.

3.4 Inserting damping material

In the previous, the muffler has been modelled as an acoustic domain consisting on the acoustic media (air) contained within the inner surface of the muffler which is modelled as a rigid wall boundary condition. With this configuration the waves are fully reflected when they interact with the boundaries of the muffler, meaning that the sound dissipation mechanism is purely reflective. However, it is desired by *Lloyd's Register* to obtain knowledge about the performance of dissipative mufflers when the exhaust system operates with different frequencies. In addition according to [Venkataraman and Raj, 2014] the gas restriction is in general lower in dissipative mufflers, which is beneficial for the compressor efficiency and therefore an interesting solution for *Lloyd's Register*. Consequently, the aim is to find muffler designs which should attenuate the sound pressure above a minimum required, with the additional consideration of being designed so that they can handle more than one working frequency. Thus, at this point the project focuses on the design of the proper distribution of absorbing material inside the expansion chamber, so that the total amount of damping material used in order to fulfil the attenuation requirements is minimum. It is crucial to provide a solution with as little damping material as possible since the materials commonly used for attenuation purposes are expensive. Before any optimum material distribution is considered, the damping material model has to be implemented in the muffler FE model. Then, this section presents the procedure followed to validate the FE model of the dissipative muffler, where the acoustic guide of ANSYS® [Acoustic Guide, 2013] has been used as a reference for building the model. In order to prove the validity of the model, the experimental results found in [Mehdizadeh and Paraschivoiu] are used for comparison.

3.4.1 Validation of damping material model

The damping material commonly used for sound attenuation consist of fibrous materials. According to [Yoon, 2012], when fibrous damping materials are used to decrease the sound pressure, the sound attenuation is governed by a complex acoustic impedance and a complex density which vary depending on the applied excitation frequency. The frequency dependent behaviour of these complex acoustic impedance and density makes it very difficult to treat acoustic attenuation with fibrous materials analytically. In this project, the attenuation effect of the fibrous material is implemented numerically in a FE model by means of the Delany-Bazley material model. This material model is the one used in the acoustic topology optimization carried out in [Yoon, 2012], furthermore this material model is available in ANSYS® for the acoustic elements FLUID 220 and FLUID 221. In addition, the Delany-Bazley material model is very simple to implement since it is an empirical material model which only needs one acoustic parameter (the so-called flow resistivity σ) in order to be applied. According to the documentation of ANSYS® [Theory Reference, 2013], the Delany-Bazley material model is limited to the working range $0.01 < f/\sigma < 1$ where f is the excitation frequency. There are other models available in ANSYS® which allow to simulate fibrous materials, one example is the Johnson-Champoux-Allard model. The Johnson-Champoux-Allard model is more difficult to implement than the Delany-Bazley model since it needs at least 5 empirical acoustic parameters, but on the other hand when the the Johnson-Champoux-Allard model is used with 5 empirical parameters and 5 additional inputs, provides more accurate results than the Delany-Bazley model. Another model available in ANSYS® is the Miki material model where the frequency working range is extended in comparison with Delany-Bazley model to $f/\sigma < 1$. The Miki material model is as simple to implement as the Delany-Bazley material model since equally than in the case of the Delany-Bazley material model, it only needs the flow resistivity σ in order to be implemented. Although the Miki material model seems more advantageous, the selection of the Delany-Bazley material model is a consequence of the information found in [Mehdizadeh and Paraschivoiu], where the Delany-Bazley material model is used to analyse a muffler similar to the one studied in this project. In [Mehdizadeh and Paraschivoiu], a 3-D finite element method is implemented in order to analyse the transmission loss in mufflers.

The validation of the FE method implemented in [Mehdizadeh and Paraschivoiu] is assessed by comparison with the experimental results presented in [Wu et al., 2002], therefore the results obtained in [Mehdizadeh and Paraschivoiu] are considered reliable.

The Delany-Bazley material model is formulated in ANSYS® according to the complex impedance:

$$Z_c = R + jX \tag{3.16}$$

and the complex propagation constant defined as:

$$\gamma = \alpha + j\beta \tag{3.17}$$

where R is the resistance, X is the reactance, α is the attenuation constant and β is the phase constant given by equations (3.18), (3.19), (3.20) and (3.21) respectively.

$$R = \rho_0 c_0 \left(1 + a\left(\frac{f}{\sigma}\right)^b\right) \tag{3.18}$$

$$X = -\rho_0 c_0 \left(c\left(\frac{f}{\sigma}\right)^d\right) \tag{3.19}$$

$$\alpha = \frac{\omega}{c_0} q \left(\frac{f}{\sigma}\right)^r \tag{3.20}$$

$$\beta = \frac{\omega}{c_0}\left(1 + s\left(\frac{f}{\sigma}\right)^t\right) \tag{3.21}$$

and the different coefficients are found in table 3.7.

Coefficient	**Value**
a	0.0497
b	-0.754
c	0.0758
d	-0.732
q	0.169
r	-0.618
s	0.0858
t	-0.7

Table 3.7: Coefficients contained in the Delany-Bazley material model.

Notice that according to these equations, the behaviour of the fibrous material is determined by the frequency ω and the flow resistivity of the material σ. Remember that $f = w/2\pi\ Hz$.

In order to validate the effectiveness of the dissipative muffler model, the axisymmetric muffler shown in figure 3.22 is modelled. This dissipative muffler is modelled with the same characteristics as the axisymmetric muffler presented in [Mehdizadeh and Paraschivoiu], therefore the goal is to obtain the same transmission loss than the obtained in [Mehdizadeh and Paraschivoiu] when the same range of frequencies is analysed.

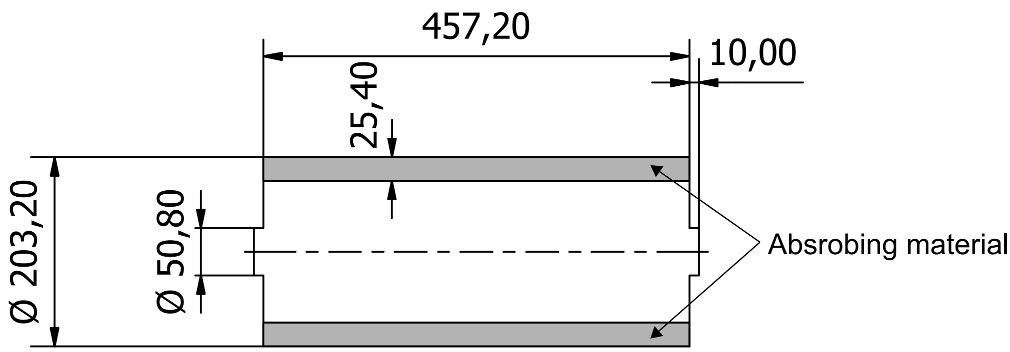

Figure 3.22: Geometry of the absorbing muffler analysed in [Mehdizadeh and Paraschivoiu]. Dimensions given in *mm*.

The absorbing material is polyester which has a flow resistivity $\sigma = 16000\, rayls/m$. The polyester lining of 2.54 *cm* of thickness is attached to the inner surface of the expansion chamber as it is represented in figure 3.22 by the grey region. The FE model is meshed in the same manner than it is done in [Mehdizadeh and Paraschivoiu] i.e. quadratic tetrahedral acoustic elements (FLUID 221 in ANSYS®) with a mesh size of 12 elements per wave length. The lengths of the inlet and outlet are not specified in [Mehdizadeh and Paraschivoiu], hence in this validation the lengths of the inlet and outlet has been chosen rather short assuming that the muffler in [Mehdizadeh and Paraschivoiu] is modelled with infinite boundary conditions ($Z = \rho_0 c_0$). The purpose of modelling short pipes is to save computational resources. The input excitation is a normal velocity corresponding to a pressure of 1 *Pa* according to equation (3.15). This normal velocity is applied on the nodes located at the initial circular cross section of the inlet.

Once the model is built with the same geometry and FE settings than the muffler presented in the literature, the analysis is run within the frequency range [100 *Hz* - 2800 *Hz*]. The curve frequency-transmission loss is shown in figure 3.24.

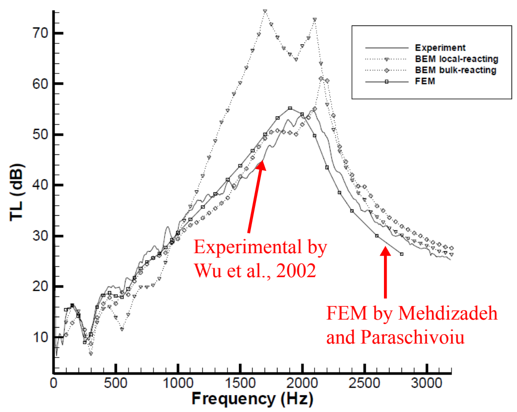

Figure 3.23: Frequency-transmission loss curve taken as reference. Figure extracted from [Mehdizadeh and Paraschivoiu, pag. 13].

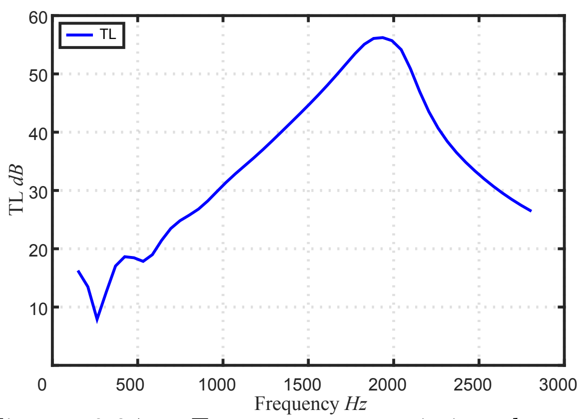

Figure 3.24: Frequency-transmission loss curve estimated by the model analysed in this project.

It is visible that the frequency-transmission loss curve shown in figure 3.24 agrees with the FEM curve obtained in [Mehdizadeh and Paraschivoiu] (figure 3.23), and therefore with the experimental curve given by [Wu et al., 2002]. Thus it is proved that the material model has been successfully implemented in the FE model and that the assumption of infinite boundary conditions at the inlet/outlet is correct.

So far, the FE model of the absorbing muffler has been validated by comparison with literature results. In the next section, the Delany-Bazley material model is implemented in the actual muffler which is object of analysis in this project.

3.4.2 Implementation of damping material model in the actual muffler

The validation of the damping material model in the previous section leads to the analysis of the muffler performance when it is modelled as a pure dissipative muffler.

The damping material simulated in the model is polyester since its flow resistivity, $\sigma = 16000\, rayls/m$, is already known from the literature. The thickness of the absorbing material is represented in figure 3.25 with grey colour, together with the dimensions of the model. Note that the length of the inlet and outlet has been reduced significantly in order to reduce the number of elements in the model. Recall that this simplification is possible due to the infinite boundary conditions applied at the inlet and outlet ($Z = \rho_0 c_0$). Tetrahedral acoustic elements (FLUID 221) are used, and the mesh size is set to $\lambda/3$ because finer meshes exceeded the limit of elements allowed by the academic license of ANSYS®. This problem with the number of elements is a consequence of the wide range of frequencies analysed ($f \in [100, 2800] Hz$) since the wave length considered in the rule $\lambda/3$, corresponds to 2800 Hz. The input excitation is the same than the excitation applied to the validation model in section 3.4.1 *Validation of damping material model.*

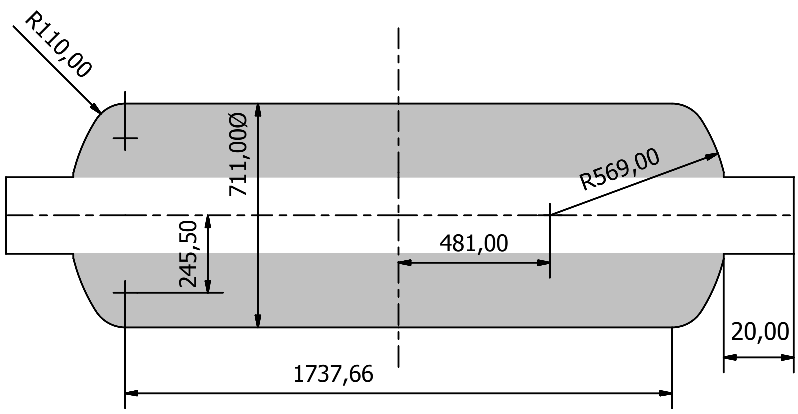

Figure 3.25: Geometry of the dissipative muffler and thickness of the absorbing lining. The dimensions are shown in mm and the scale is not real.

The transmission loss curve obtained from the execution of the model is represented in figure 3.26.

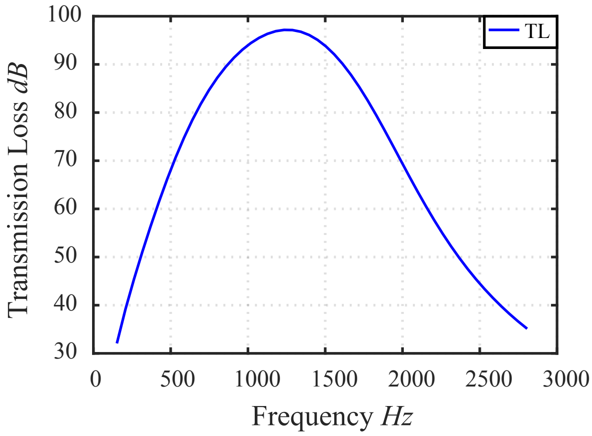

Figure 3.26: Frequency - transmission loss curve extracted from the analysis of the dissipative muffler.

It is seen in figure 3.26 that the transmission loss is very high for all the frequencies considering that the requirement established by *Lloyd's Register* is a sound attenuation of 17 dB. The high transmission loss obtained is obviously a consequence of the thick lining of polyester which has been considered in the analysis. This fact demonstrates that placing the absorbing material by trial and error could lead to increase the material cost unnecessarily, hence it becomes convenient to figure out a way of distributing the damping material efficiently. In the next chapter the problem of optimising the applied absorbing material is dealt.

Optimisation of muffler 4

A numerical model of the muffler has been created in the previous chapter which allows for the optimisation process to begin. For convenience the objective of the optimisation is now repeated in the following.

The assignment set forth by *Lloyd's Register* consists of creating a MATLAB optimisation tool which allows for the optimisation of a muffler used mainly for maritime operations. The demands for the optimisation is to reduce the the amount of absorbing material applied to achieve an attenuation of the sound, equivalent to a transmission loss of at least 17 *dB*.

It was requested by *Lloyd's Register* to secure this attenuation throughout the etire spectrum of frequencies until 2000 *Hz*, but through a mutual agreement, the range has been reduced to three discrete frequencies; a fundamental driving frequency at 446 *Hz* and the 2nd and 3rd harmonics of the driving frequency at 892 *Hz* and 1338 *Hz* respectively.

The general optimisation problem is formulated as:

$$\textit{Minimize:} \quad f = m \quad \text{where} \quad m = V \cdot \rho_{damp} \tag{4.1}$$

$$\textit{Subject to:} \quad g_j = 17 - TL_j \leq 0; \quad j = [1,2,3] \tag{4.2}$$

It is of great concern to ensure that the optimisation will provide a design which is manufacturable, meaning that voids in the damping material must not be present in the final design. This must be taken into consideration when choosing an optimisation method.

In the following section the general types of structural optimisations are briefly introduced and discussed with the aim of choosing one method for application on the problem at hand.

4.1 Types of optimisations

As the general optimisation problem has been identified, the type of optimisation applied to the problem is discussed. Generally three methods exist for optimisation of structures; sizing, shape and topology optimisation. Now continues a very brief introduction to each optimisation method is given in the following.

Sizing optimisation uses a predefined structure and sets to determine individual dimensions in order to fulfil the objective of the problem. The design variables typically chosen for sizing optimisation are length, thickness or area and the final design will therefore also be of the same predefined shape, illustrated on figure 4.1. This method can be applied on the muffler design to determine the thickness or the inner diameter of the damping material.

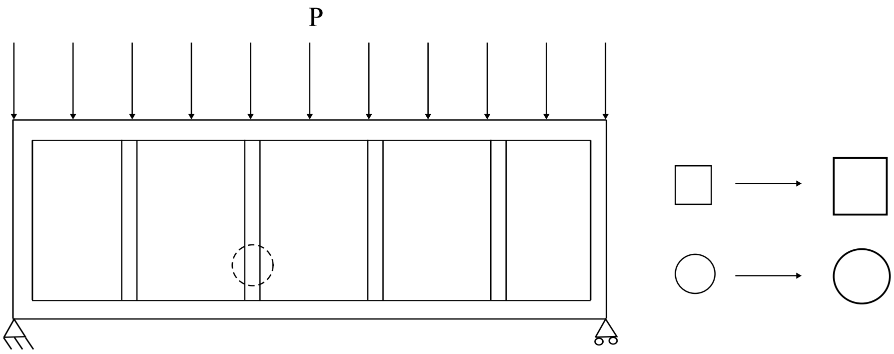

Figure 4.1: The principle of sizing optimisation.

Shape optimisation relies on individual points where the design is allowed to change and is most often combined with finite element models. When applying shape optimisation in conjunction with finite element model, relevant nodes are used as design variables by assigning them a degree of freedom, e.i. a certain path they must follow. From here a new design can be determined. The final design is dependent and thus limited to which nodes are chosen as design variables, see figure 4.2.

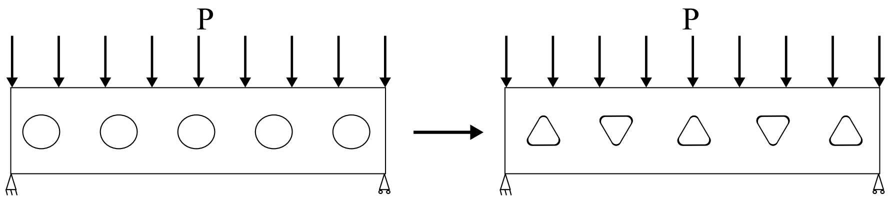

Figure 4.2: The principle of shape optimisation.

The objective of the topology optimisation, is to yield the optimal material distribution not constrained by initial parametrizations but only limited by initial design space, boundary conditions and loads. Topology optimisation uses densities as design variables in a discretized design domain, e.i. an FE model. The design variables scales the material properties on an element basis, most commonly used in the scaling of Young's modulus E, for the minimisation of compliance in a load bearing structure. Ideally these design variables are either zero or one, which is interpreted as inactive or active elements respectively. However, as many optimisation methods rely on gradient information, the element densities needs to be continuous rather than discrete variables. The intermediate density scaled material parameters are often illustrated using grey-scaled colors, where white is no material (inactive) and black is full material (active). Anything in between is shown in grey-scale.

Topology optimisation is generally the first step of a structural optimisation and relies on refinement from either sizing optimisation or shape optimisation. Post processing of the topology optimisation is also in most cases needed to achieve proper discreteness of the material.

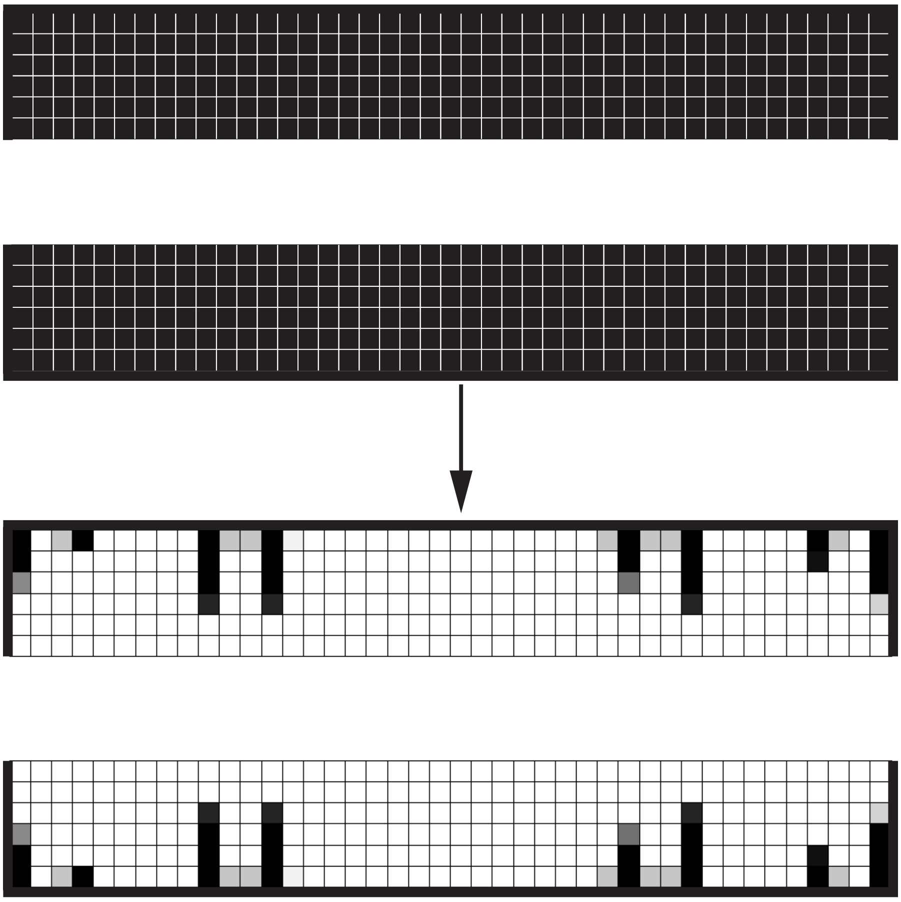

Figure 4.3: The principle of topology optimisation applied on a muffler.

It is of interest for *Lloyd's Register* to obtain knowledge about the advantages of applying topology optimisation in order to recieve design candidates for the distribution of absorbing material inside the muffler.

4.2 Choice of optimisation solver

It has been clarified that topology optimisation has been chosen for this project as a mean to reduce and redistribute the absorbing material used in dissipative mufflers.

The specific solver for the optimisation problem must be chosen, and the choice now stands between two main branches of numerical optimisation methods; heuristic and gradient based optimisers. The two are vastly different and will in the following be shortly introduced.

Heuristic optimisation methods, also known as genetic solvers, relies on the evaluations of different designs, often initially generated randomly to create a so-called generation. The random designs are then compared. The best design of one generation, is used as basis of creating new designs within a certain range of the best design from the previous generation. This way a vast number of different design combinations can be evaluated but the trade-off is that they must often use many iterations to converge at a minimum, when compared to gradient based optimisers.

However, as the heuristic methods initially branches a vast number of possible design combinations at once, it can be a very effective tool, when combined with gradient based solvers to determine initial design suggestions.

As the name suggest, gradient based solvers relies on gradient information about the considered problem. This means, in very basic terms, that a prediction is made of how the problem will behave, by evaluating the gradient of both objective function and constraints at a certain design suggestion. A new design can then be determined from the direction which minimises the objective function.

For the particular problem of this project the *Sequential Linear Programming* or SLP method has been chosen, partly because an implemented SLP optimisation algorithm was readily at hand. The SLP method is a relatively simple method as it relies on a linearisation of both objective function and constraints creating what is called the *linearised sub problem*. In other words, the linearised sub problem predicts the behaviour of the system based on the gradient information in the current design point. *Move limits* are applied to the sub problem which ensures that the prediction is contained in close proximity to the initial design point. Adaptive move limits are often applied, which will increase or decrease the move limits depending on the progress of the optimisation. This helps to reduce the risk of violating constraints. The SLP method is not particularly advanced or quick, but it is a very robust method which works for most problems.

Another gradient based method known as the *Method of Moving Asymptotes* [Svanberg, 1987] or MMA has been considered. The method resembles the SLP method but instead of a purely linear prediction of the system's behaviour, the gradient information is used to construct a second order approximation at the current design point by applying convex functions governed by lower and upper limits known as asymptotes. The second order approximation at the design point is modified in each iteration by moving the asymptotes, in the same fashion as the move limits of the SLP method. This means that MMA is often much faster to converge than the SLP method, as the prediction is of second order, though it will depend on the problem at hand as stated in [Svanberg, 1987].

As the choice of solver is the SLP method, a more in-depth description of the method is presented in the following section.

4.2.1 Sequential Linear Programming

A slightly more in-depth explanation of the SLP method is now presented. The SLP method is in short, an iterative process where a linear sub problem is constructed based on a design point $\mathbf{x}^{(k)}$ of iteration k. Where $\mathbf{x}^{(k)}$ is a vector containing all design variables. The sub problem consists of a linearisation of the objective function and the constraints in the current design point.

Consider now the evaluation of a new design point $\mathbf{x}^{(k+1)} = \mathbf{x}^{(k)} + \Delta\mathbf{x}^{(k)}$ approximated using a first order Taylor expansion of both objective function and constraints in the current design $\mathbf{x}^{(k)}$.

$$f(\mathbf{x}^{(k)} + \Delta\mathbf{x}^{(k)}) \cong f(\mathbf{x}^{(k)}) + \nabla f^T(\mathbf{x}^{(k)})\Delta\mathbf{x}^{(k)} \tag{4.3}$$

$$g_j(\mathbf{x}^{(k)} + \Delta\mathbf{x}^{(k)}) \cong g_j(\mathbf{x}^{(k)}) + \nabla g_j^T(\mathbf{x}^{(k)})\Delta\mathbf{x}^{(k)} \leq 0 \qquad j = [1,2,3] \tag{4.4}$$

Where $\nabla f^T(\mathbf{x}^{(k)})$ and $\nabla g_j^T(\mathbf{x}^{(k)})$ are the gradients of the objective and inequality constraints respectively, evaluated at the current design point $\mathbf{x}^{(k)}$.
$\Delta\mathbf{x}^{(k)}$ is the *step size* or the change of design variables needed for a reduction in the objective function value.

The linearisation provides and approximation of the value of both objective function and constraints at the new design point $\mathbf{x}^{(k+1)}$.

However, since the problem dealt with in this project does not have any explicit expressions for determining the transmission loss (TL), the constraint evaluation and the gradient information must be calculated through an FE analysis. The gradient approximation using forward/backward difference through a design sensitivity analysis will be described in more detail in section 4.4.3.

The linear sub problem is now introduced. The sub problem consists of the approximated gradient information to set up a number of linear equations for which the step size $\Delta\mathbf{x}^{(k)}$ is determined.

$$\textit{Minimise:} \quad \overline{f} = \sum_{i=1}^{n} \nabla f^T(\mathbf{x}^{(k)})\Delta x^{(k)} \tag{4.5}$$

$$\textit{Subject to:} \quad \sum_{i=1}^{n} \nabla g_j^T(\mathbf{x}^{(k)})\Delta\mathbf{x}^{(k)} \leq g_j(\mathbf{x}^{(k)}); \quad j = [1,2,3] \tag{4.6}$$

With the linear sub problem defined, the collection of linear equations can now quickly be solved with respect to the step size $\Delta\mathbf{x}^{(k)}$ which will minimise the objective function. Note that the step size is limited by the choice of move limits. Traditionally the move limits are chosen as a certain percentage of the current design but is changed then changed as per iteration depending on the objective function value. The adaptive move limit strategy for the problem at hand is explained in more detail in section 4.4.6.

The newly determined design $\mathbf{x}^{(k+1)} = \mathbf{x}^{(k)} + \Delta\mathbf{x}^{(k)}$ is applied as the initial design for the next iteration and the process is repeated.

Normalisation of the constraints

It is known as good practice to normalize the constraints to avoid numerical problems during evaluation of the constraints. Normalising the constraints from equation (4.2) related to the problem at hand, yields equation (4.7).

$$g_i\left(\mathbf{x}\right) = -\frac{TL_i\left(\mathbf{x}\right)}{17} + 1 \leq 0 \tag{4.7}$$

In the instance of constraints with vastly different magnitudes, it is especially convenient to have normalised constraints.

It has now been chosen to apply topology optimisation with a solver based on the *sequential linear programming* scheme. As the problem at hand is inherently implicit, an FE analysis must be carried out to determine the effect on the transmission loss with respect to constraints evaluations. This motivates a development of a FE model with an easily accessible design space. The FE model for the topology optimisation will be based upon the findings in chapter 3.

4.3 Absorbing model adapted for optimization

As the constraint evaluation and constraint design sensitivity analysis needs to run the FE model in order to obtain the transmission loss, this section presents the final FE model of the muffler which is used in the optimization process. All the considerations taken into account in order to make the model suitable for the optimization process are described.

4.3.1 The final FE muffler model

The final model used in the optimisation consist on a 3-D acoustic FE model, which uses the Delany-Bazley material model in order to simulate the effect of the absorbing material (Polyester). The decision of using a 3-D model relies on the fact that the Delany-Bazley material model is only available in ANSYS® for 3-D acoustic elements. However, even computationally expensive, using a 3-D model has an important advantage, which is that mixed modes are not an issue since 3-D acoustic elements capture wave propagation in all directions.

Consider, the geometry of the final model which is intended to be used in the optimisation process, shown in figure 4.4. It has been decided to keep the round walls with the aim of modelling the muffler as close as possible to reality. However the fact of having round walls increases the complexity of the element manipulation as it is discussed in the next section.

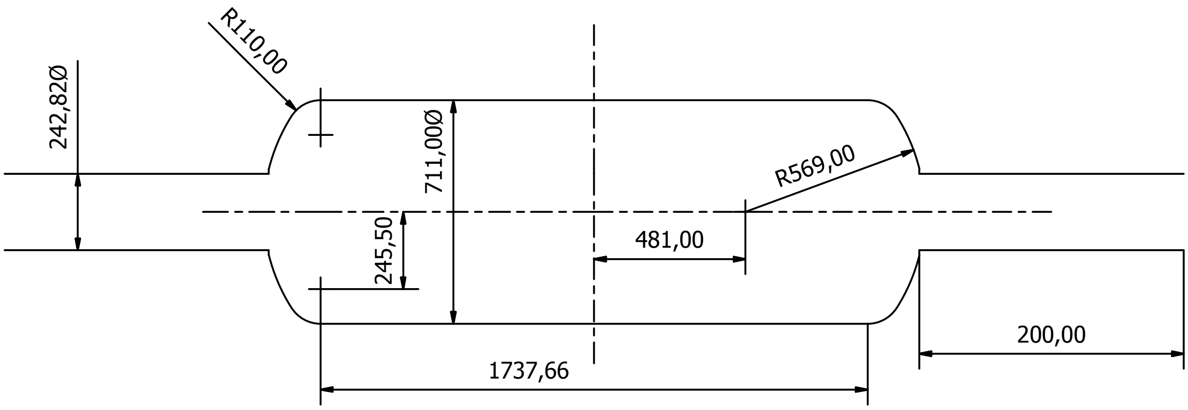

Figure 4.4: Dimensions in mm of the final model. The scale shown in the figure is not real.

Similarly to the previous models, the inlet and outlet are assumed to be bounded at infinity i.e Sommerfeld boundary condition[1] is applied. The input excitation is a normal velocity corresponding to a pressure of 1 Pa according to equation (4.8) which is applied in the nodes located in the inlet. Daniel Rey Romero Note!

$$v_n = \frac{p_i}{\rho \cdot c_0} \tag{4.8}$$

Regarding the element technology used so far, only tetrahedral elements have been employed since it is easier to mesh complex geometries with these kind of elements. Nevertheless topology optimization requires element manipulation because each element represents a design variable, therefore the next section presents how the mesh is adapted in order to be suitable for topology optimization.

4.3.2 Adapting the mesh for optimization

First of all it is important to present an important decision which has been taken regarding the choice of the design space. Since the FE optimisation model is 3-D, carrying out a 3-D topology optimisation might become computational expensive if many design variables (elements) are contained in the design space. This computational issue would be a consequence of the design sensitivity analysis[2] since it might require many more function evaluations. Taking this into account, it is desired to simplify the design space by considering the 2-D design space illustrated in figure 4.5 (top). Then whenever the optimiser dictates that one design variable (element) needs to change, all the elements located at the same radial position change accordingly as it is sketched in figure 4.5 (bottom). This way the amount of function evaluations which need to be performed is reduced considerably. In addition note in figure 4.5 that the regions close to the rounded edges are neglected, this simplification is further commented in the following. Daniel Rey Romero Note!

[1]Daniel Rey
Romero Note: add Sommerfeld boundary in TLA

[2]Daniel Rey
Romero Note: this have to be mentioned when presenting SLP

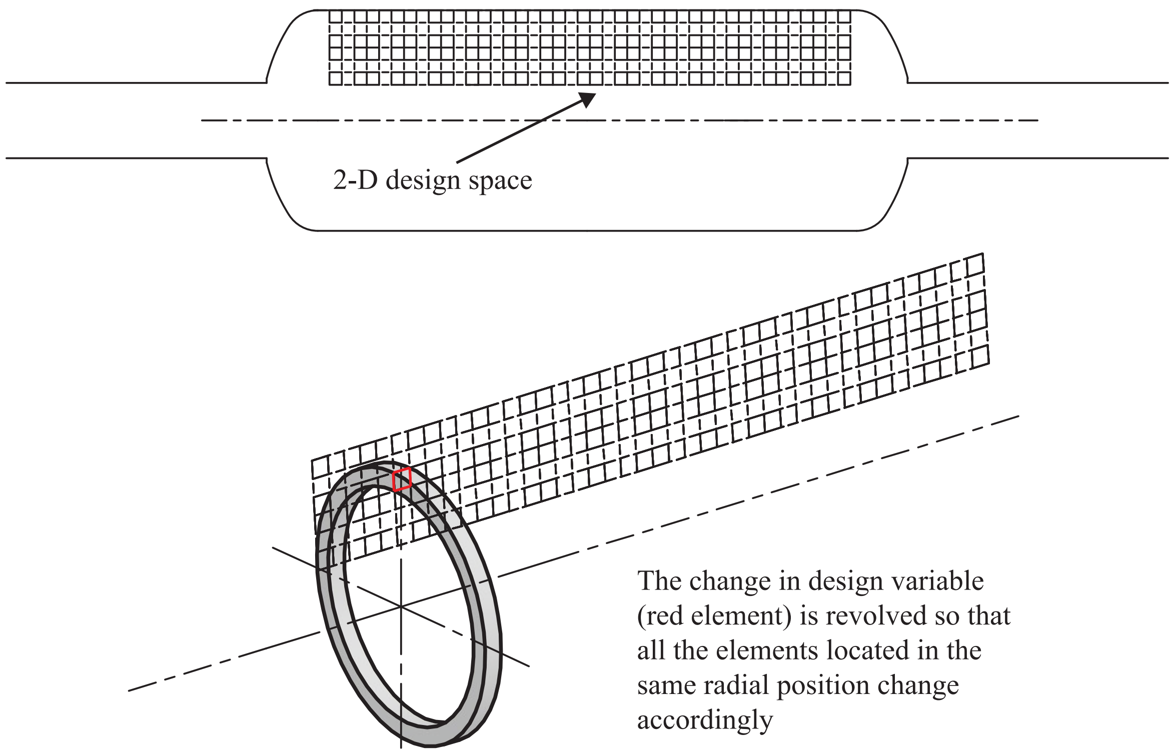

Figure 4.5: Graphical representation of the proposed design space.

It becomes clear that topology optimization needs element manipulation. Basically the material properties of the elements contained within the design space need to change when the optimizer dictates that the current design must be updated. Consequently it is essential to know the element number and the element location within the design space. Furthermore since the objective is to reduce mass, it is necessary to know the element volume as well. It turns out that it is very difficult to fulfil all these mesh requirements with a mesh formed by tetrahedral elements since, it is hard to find specific elements in the mesh. Due to this reason, the element technology is changed to hexahedral acoustic elements (FLUID 220) so that it is possible to generate a mapped mesh in the design space as it is represented in figure 4.6, within the region inside the red lines. Note that figure 4.6, that for simplicity, the regions next to the round walls are excluded from the design space since the element have random locations and distorted shapes. Considering these regions where the elements are distorted and not organised according to a established sequence, would complicate considerably the element manipulation. In order to get a mapped mesh in the design space the procedure followed is described below:

- The areas corresponding to the design space are selected.
- The selected areas are attributed with absorbing material properties and meshed afterwards with an element size corresponding to 6 elements per wave length. The highest driving frequency is chosen to establish the element size as it would provide an adequate mesh size for all the driving frequencies.
- After the design space is meshed (region bounded by the red lines in figure 4.6), the rest

of areas are selected. These areas are attributed with air material properties and meshed afterwards with the same element size than the absorbing region. It is very important to mesh the design space before the rest of the domain. Following this order the design space is meshed with square elements while the rest of the domain is meshed with square elements when it is possible. However distorted quadrilateral elements are generated in regions where the geometry is rather complicated. If the areas are meshed in a different order, mesh connectivity problems might occur.

- Once the 2-D mesh is generated, the result looks like the mesh shown in figure 4.6). Finally the 2-D mesh is revolved so that 40 elements in total are generated along 360°. The final mesh is shown in figure 4.7.

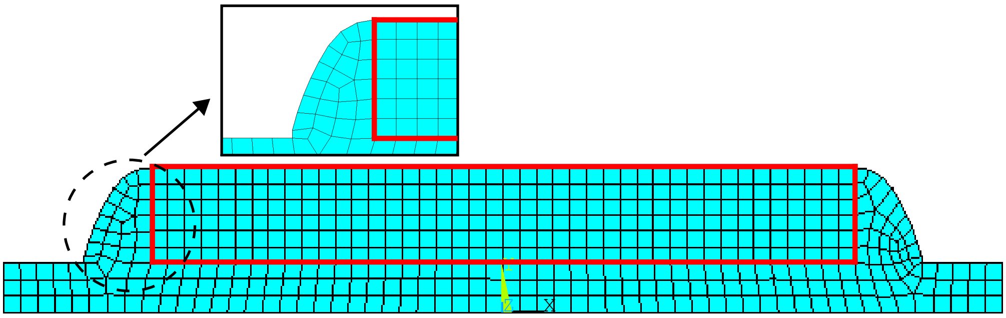

Figure 4.6: 2-D mesh generation.

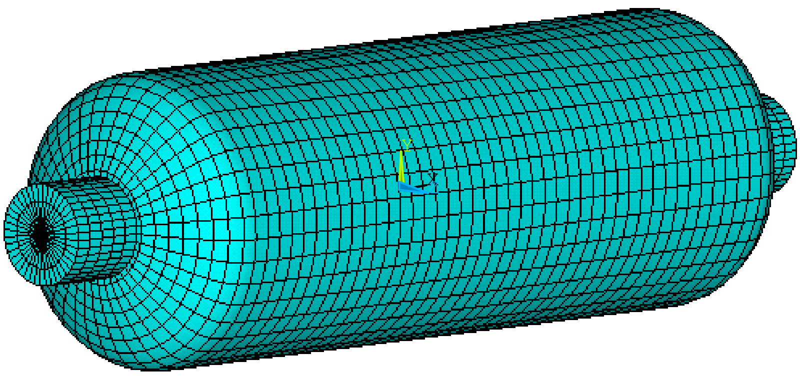

Figure 4.7: Final mesh generated with hexahedral acoustic elements FLUID 220.

After the mesh of the model has been adapted for topology optimization, the next issue to discuss is how the mesh is manipulated during the optimization.

4.3.3 Element manipulation

First of all, remember that in order to simplify the optimization, the 2-D design space shown in figure 4.8 is considered even though the optimization relies on a 3-D FE model. Each element in the design space constitutes a design variable which may change its material property during the optimization i.e. either the element remains being absorbing material or the element becomes air. This means that initially each element is attributed with a flow resistivity $\sigma = 16000\, rayls/m$ and an element density $\rho_{el}^{(i)} = 1$ where $i \in [1,ne]$. The element density $\rho_{el}^{(i)}$ must be understood as a factor given by the optimizer which defines whether the element should be absorbing material or air. The basic idea is that the element becomes air if σ is multiplied by $\rho_{el} \to 0$ and the element remains as absorbing material if σ is multiplied by $\rho_{el} = 1$. As an illustrative example of this, let us remember the expression of the resistance defined according to the Delany-Bazley material model where the effect of the element density ρ_{el} has been included:

$$R = \rho_0 c_0 \left(1 + 0.0497 \left(\frac{f}{\rho_{el}\sigma} \right)^{-0.754} \right) \tag{4.9}$$

Consider that the optimizer provides an element density $\rho_{el} = 1 \cdot 10^{-9}$ which multiplies the flow resistivity in equation (4.9) so that the term $\frac{f}{\rho_{el}\sigma}$ becomes a very large number because f is divided by a number approaching zero (f can never be divided by zero in order to avoid numerical singularities). This large number to the power of -0.754 results in a number which approaches zero. In conclusion if $\sigma \to 0$ it is obvious that $R \approx \rho_0 c_0$, which means that the element does not offer resistance to the air since $\rho_0 c_0$ is the Sommerfeld radiation principle. This example only is shown for illustrative purposes, in the optimization algorithm σ and the element density ρ_{el} are related by means of either the SIMP or RAMP scheme given in equations (4.14) and (4.15) respectively. In order to attribute a density design variable to each element inside the design space, the sequence of element number in the model is considered as explained in the following.

The design space is formed by 6 rows of elements and 42 columns of elements which yields a total of 252 element design variables $\rho_{el}^{(i)}$ where $i \in$ [1,252]. These element densities are stored in a vector of dimension 252 according to element numbering shown in figure 4.8.

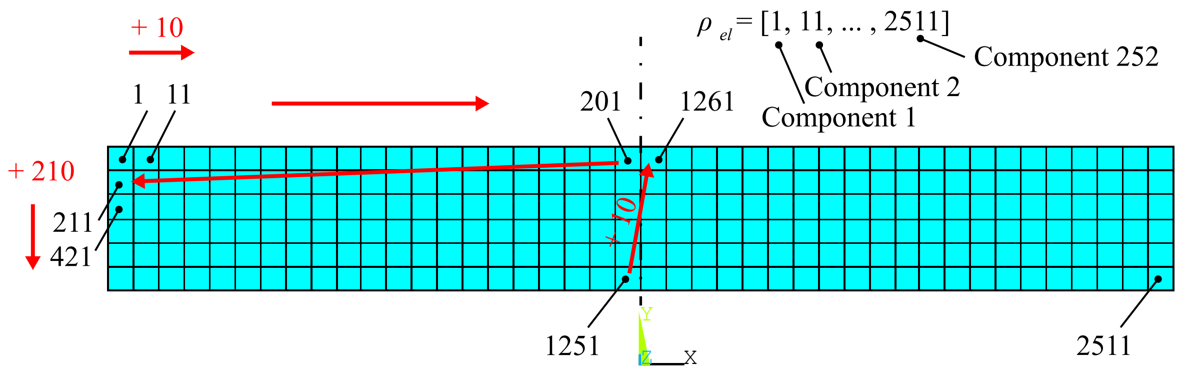

Figure 4.8: Element numbering sequence in the design space.

Another consideration that must be taken into account, is that whenever the element density is updated, all the elements which result of revolving the element design variable (marked in red in figure 4.9) change accordingly as represented in figure 4.9. Therefore it is essential to know the sequence of the element numbers in the group of element formed by elements located at the same radial position, see figure 4.9.

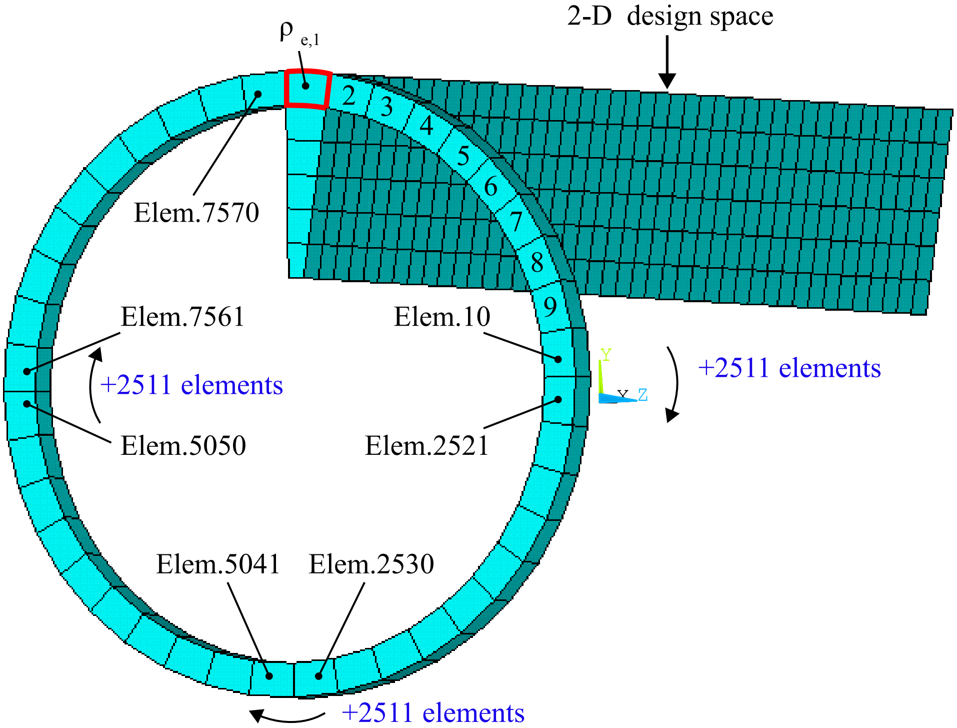

Figure 4.9: Representation of the group of elements corresponding to one design variable.

At this point, the FE model is prepared so it can change the element material properties according to the new designs provided by the optimiser. Provided with a tool for constraint evaluation and constraint sensitivity analysis, the optimisation procedure is presented in the following.

4.4 Optimisation procedure

So far, it has been decided to optimise the absorbing material in the muffler by using gradient based topology optimisation. Then, sequential linear programming is chosen to solve the topology optimisation problem and the FE model of the muffler has been adapted to the topology approach since this model is necessary in order to evaluate the constraints. All this, leads to the description in details of the process followed to solve the topology optimisation problem.

4.4.1 The thickness filter

The optimisation model presented in the previous section constitutes a tool which allows to evaluate the constraints as it provides the transmission loss in the system. All elements present in the design space are subject to change during the optimisation, where an element can either be air or damping material. The material distribution inside the design space will greatly influence the transmission loss. It is important to remember that the objective is to minimize the mass of damping material while still having a minimum sound reduction through the system, but it is also important to attain a solution which is easy to manufacture. To avoid complexity due to discontinuity in patches of damping material, it is desired to use the idea of casting constraints. A thickness filter was developed in [Sørensen and Lund, 2015] which uses a reformulation of the projection filter developed by [Wang et al., 2011]. This thickness filter introduces a new design variable ρ_c, which represents columns of elements in the design space. This is represented in figure 4.10.

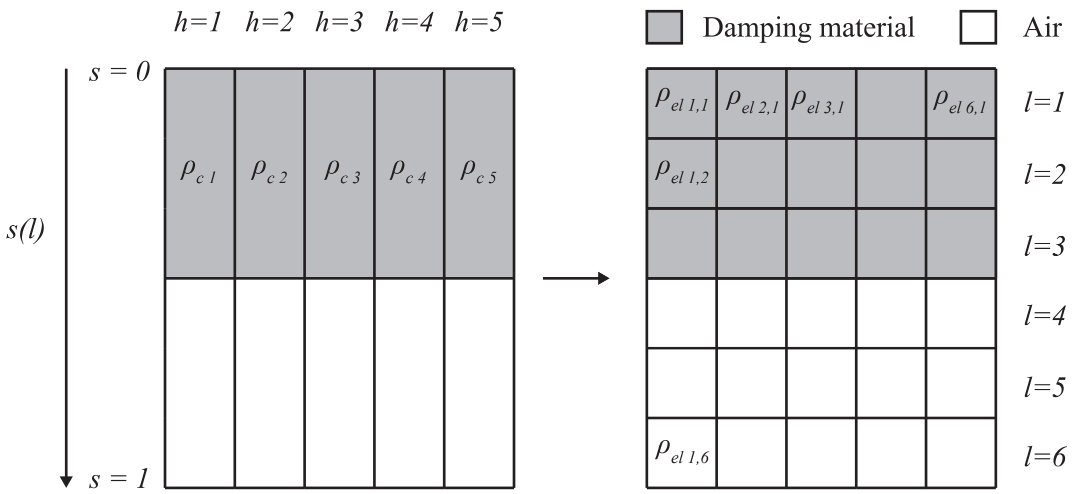

Figure 4.10: Representation of the column design variables and the mapping of the column variables onto the element design variables.

The reason to introduce column densities is to ensure the absent of voids in the patches of damping material. The optimiser only understands column densities, but in order to evaluate the constraints, the real design variables needs to be determined. Hereby, the element densities are determined from the expression of the thickness filter, equation (4.10) (found in [Sørensen and Lund, 2015]), which are then mapped onto the real model.

$$\rho_{el}^{(i)} = 1 - \frac{tanh\left(\beta \cdot \rho_c^{(h)}\right) + tanh\left(\beta \cdot \left(s(l) - \rho_c^{(h)}\right)\right)}{tanh\left(\beta \cdot \rho_c^{(h)}\right) + tanh\left(\beta \cdot \left(1 - \rho_c^{(h)}\right)\right)} \tag{4.10}$$

Where $h = 1 \ldots n_c$ is the column number. β is the steepness of the filter. $s(l)$ is a, through-the-thickness, normalized coordinate system where l is the element number in the column and n^l is the total number of elements per column. An expression for $s(l)$ can be seen on the following equation.

$$s(l) = \frac{(l-1)}{n^l} + \frac{1}{2n^l} \tag{4.11}$$

In order to illustrate the mapping of element densities from column densities, half of a column density is considered ($\rho_c^{(h)} = 0.5$). By applying $\rho_c^{(h)} = 0.5$ to equation (4.10) the curve shown in figure 4.11 is obtained.

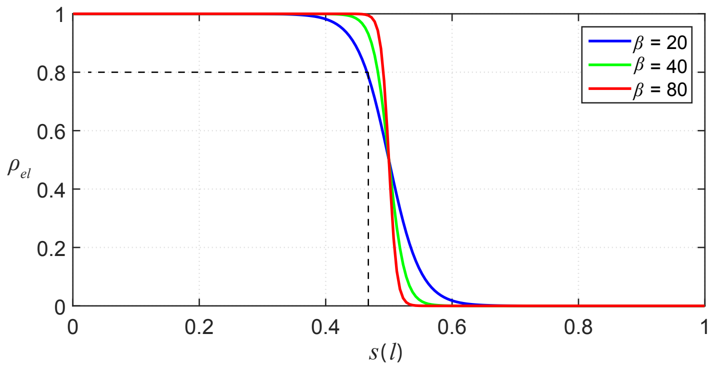

Figure 4.11: Graph showing the effects of β for the thickness filter.

It is visible in figure 4.11 that thickness coordinates next to the column density values will never provide discrete element densities as represented in the figure by the dashed black line. It can be seen as well, that by increasing β the discreteness of the element density will increase. As the physical design variables (elements) are dependant on the column densities a new expression has to be considered in the sensitivity analyses, a general expression for the sensitivity analyses can be seen on equation (4.12).

$$\frac{\partial f}{\partial \rho_c} = \frac{\partial f}{\partial \rho_{el}} \cdot \frac{\partial \rho_{el}}{\partial \rho_c} \tag{4.12}$$

Where the second term is the derivative of equation (4.10) with respect to the column density. It is important to note that equation (4.12) is a general expression and f should not be confused with the objective function, rather consider it a general function. The second factor in equation (4.12) is illustrated in figure 4.12 using the same values of β as figure 4.11.

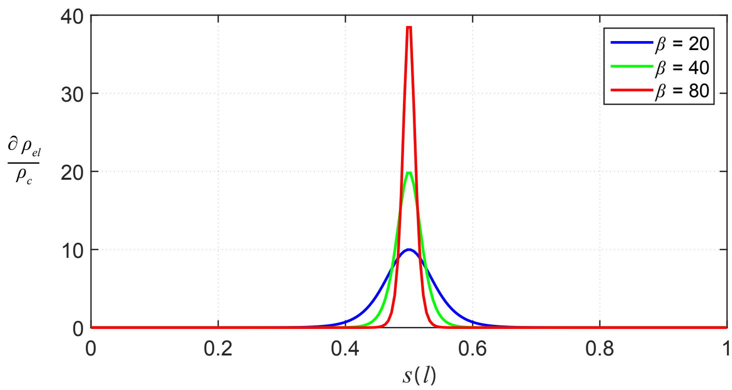

Figure 4.12: Graph showing the sensitivity of the thickness filter.

It can be seen that by increasing β might yield a more discrete solution, but will give a poorer linear prediction as the gradient is very steep. The discreteness of the design can be determined from the following expression, suggested in [Sigmund, 2007].

$$M_{dnd} = \frac{4 \cdot \sum_{d,l} V_{el}\rho_{el} \cdot (1 - \rho_{el})}{\sum_{d,l} V_{el}} \tag{4.13}$$

Now that the link between column densities and element densities has been determined, the interpolation of design variables can be applied.

4.4.2 Interpolation and penalization

When working with topology optimisation it is important to note that it is desired to acquire a purely binary solution. However, as the optimisation of the muffler is conducted using a gradient based optimisation it is important to interpolate the design. This relaxes the design variables from purely binary to a range variable $0 \leq \rho_{el} \leq 1$. The interpolation of the design is done using two different methods to investigate the consequence of the interpolation of a design in acoustic domain. The interpolation schemes can be seen in equation (4.14) and equation (4.15).

$$\sigma = \sigma_0 + \rho_{el}^p (\sigma - \sigma_0) \tag{4.14}$$

$$\sigma = \sigma_0 + \frac{\rho_{el}}{1 + p(1 - \rho_{el})} (\sigma - \sigma_0) \tag{4.15}$$

Where equation (4.14) is the SIMP scheme and equation (4.15) is the RAMP scheme. σ_0 is set to be a very small number so if $\rho_{el} = 0$ no problems occur from dividing by zero. By investigation $\sigma_0 = 10^{-9}$ has been sufficient in representing air when $\rho_{el} = 0$.
Even though the thickness filter is applied, a fully discrete solution is not guaranteed. Because the filter is curved it might result in non-discrete values where elements are close to the column value even if $\beta \to \infty$. Penalization of the design variable is applied to force the optimiser to settle on a solution of the column densities which yields discrete solutions of the element densities.
A penalization of $p = 3$ for SIMP scheme is well established penalization in optimisation of compliance. As the design variable has an extra exponent due to the Delany-Bazley formulation, equation (4.16) is considered to acquire a penalization factor which is coherent with traditional optimisations.

$$\rho_{el}^3 = \left(\frac{1}{\rho_{el}^p}\right)^{-0.754} \tag{4.16}$$

Equation (4.16) is considered at $\rho_{el} = 0.5$ as the solution will be least discrete at this point, and $p = 4$ is determined. A study of the traditional SIMP with the equivalent SIMP where $p = 4$ equation (4.16) was performed. It can be determined from figure 4.13 that the two penalizations are equal for every $\rho_{el} \in [0,1]$.

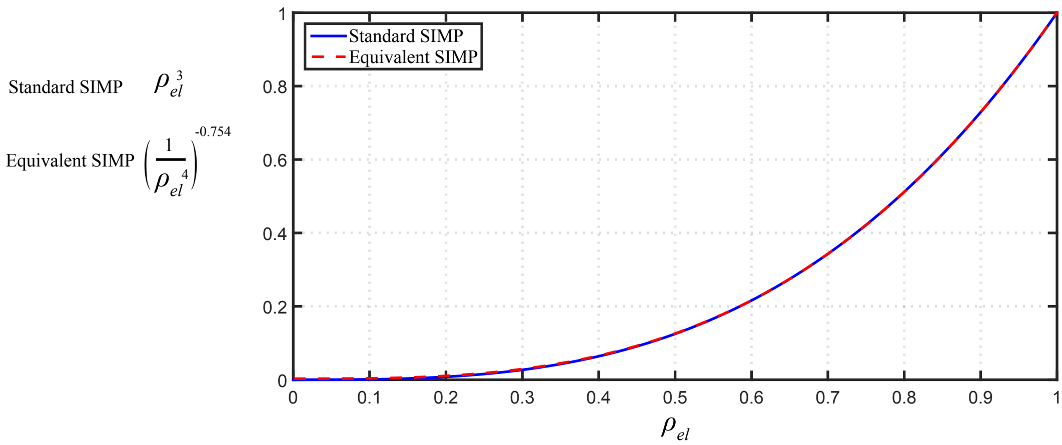

Figure 4.13: Plot of the general SIMP and equivalent SIMP from equation (4.16), where $p = 4$, with blue and red line respectively.

A series of penalization factors for the SIMP method was chosen for investigation. The motivation for this is to determine sufficient penalization coefficients for the optimisation if $p = 4$ would prove not sufficient. The effects from investigated penalization coefficients can be seen on figure 4.14.

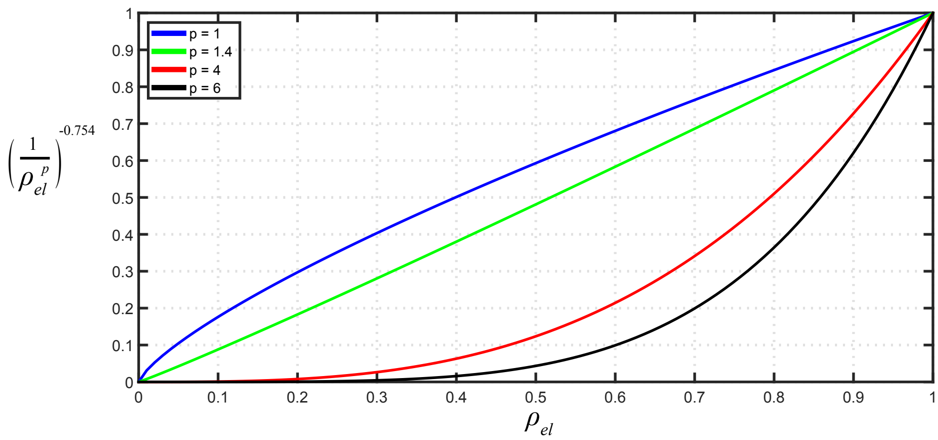

Figure 4.14: SIMP method penalizations modified for Delany-Bazley model.

It is important to use a penalization curve where the curvature is smooth. By applying a curve which resembles a step function, the linear prediction of a new design variable will be poor. By applying the same the though process to determine the penalization coefficient between SIMP and RAMP scheme, $p = 14$ was found. However, by comparing the SIMP curve with the RAMP curve with equal penalization it can be seen from figure 4.15 that the penalisation is only equal at $\rho_{el} = [0.0\ ,\ 0.5\ ,\ 1.0]$.

A couple of penalization curves were investigated using RAMP method, seen on figure 4.16. The idea is to gain knowledge about the parametrisation of the RAMP method.

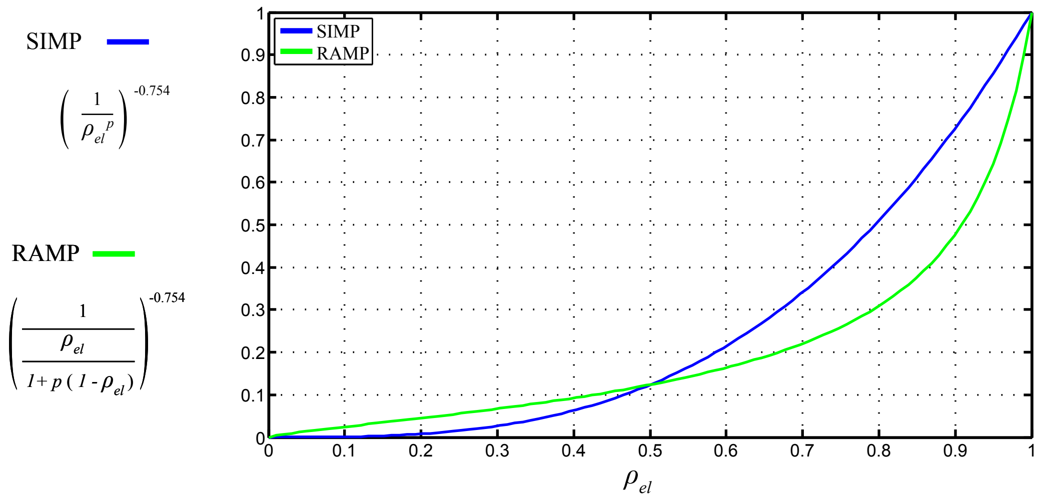

Figure 4.15: Comparison between SIMP and RAMP penalization where $p = 4$ and $p = 14$ respectively.

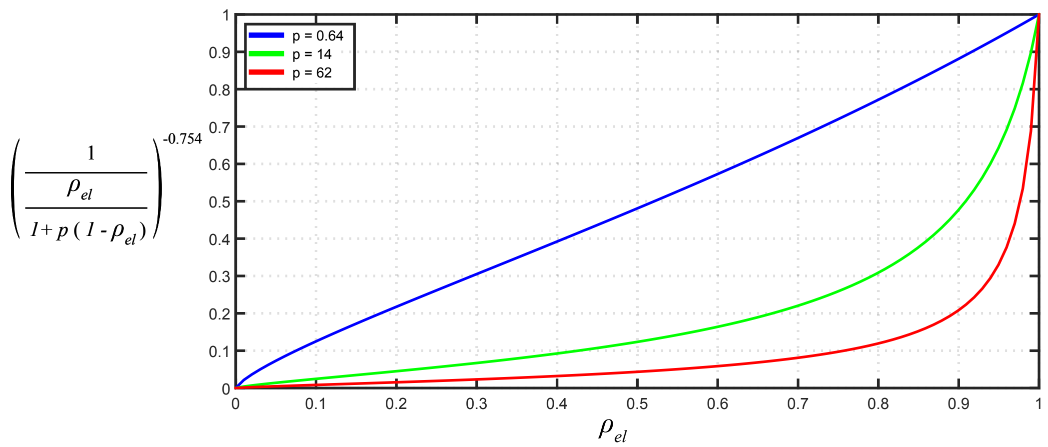

Figure 4.16: RAMP method translated from SIMP penalizations for Delany-Bazley model at $\rho_{el} = 0.5$.

The RAMP scheme tend to has a weaker penalization towards a function value of zero. However, when $\rho_{el} < 0.5$ the RAMP scheme has a better curvature than SIMP. Both interpolation schemes will be tested during the optimisation process where findings will be discussed later in the report.

As the design variables are relaxed and becomes continuous, a penalization is applied to force the solution towards a discrete solution. Now that the problem is suitable for gradient based optimisation the processes of determining the gradients of the design can be performed. This is explained further in the following subsection.

4.4.3 Gradient approximation

Because the optimiser is gradient based, the derivative of the objective function and constraints needs to be determined. As the objective function is an explicit analytical equation the gradient can easily be determined. However, the transmission loss can not be explicitly expressed so a forward and backward difference approximation is used. Forward or backward difference is used over central difference as central difference would need twice the function evaluations, consequently it would double the computational time. The expressions for the gradients can be seen on equation (4.17), equation (4.18) and equation (4.19). In these equations, the terms of the chain rule involving the transmission loss TL are the ones which are calculated by difference approximations, therefore ANSYS® is executed in order to estimate these terms for each design variable $\rho_{el}^{(i)}$.

$$\frac{\partial m}{\partial \rho_c^{(h)}} = \frac{\partial m}{\partial \rho_{el}^{(i)}} \cdot \frac{\partial \rho_{el}^{(i)}}{\partial \rho_c^{(h)}} \tag{4.17}$$

$$\frac{\partial\, g\left(\omega_j\right)^{(forward)}}{\partial \rho_c^{(h)}} = \frac{\partial\, g\left(\omega_j\right)^{(forward)}}{\partial \rho_{el}^{(i)}} \frac{\partial\, \rho_{el}^{(i)}}{\partial \rho_c^{(h)}} = -\frac{1}{17} \frac{TL\left(\rho_{el}^{(i)} + \delta\rho_{el}^{(i)}\right) - TL\left(\rho_{el}^{(i)}\right)}{\delta\rho_{el}^{(i)}} \frac{\partial\, \rho_{el}^{(i)}}{\partial \rho_c^{(h)}} \tag{4.18}$$

$$\frac{\partial\, g\left(\omega_j\right)^{(backward)}}{\partial \rho_c^{(h)}} = \frac{\partial\, g\left(\omega_j\right)^{(backward)}}{\partial \rho_{el}^{(i)}} \frac{\partial\, \rho_{el}^{(i)}}{\partial \rho_c^{(h)}} = -\frac{1}{17} \frac{TL\left(\rho_{el}^{(i)}\right) - TL\left(\rho_{el}^{(i)} - \delta\rho_{el}^{(i)}\right)}{\delta\rho_{el}^{(i)}} \frac{\partial\, \rho_{el}^{(i)}}{\partial \rho_c^{(h)}} \tag{4.19}$$

$h \in [1{,}42] \qquad i \in [1{,}252] \qquad j \in [1{,}3]$

It is important to clarify that the derivative of the constraint with respect to the element design variable $\rho_{el}^{(i)}$ is performed either by forward or backward difference but not both of them. The criterion which dictates which method is used each time is shown below:

If $\rho_{el}^{(i)} - \delta\rho_{el}^{(i)} \leq 0$ **then**
Forward difference
Else
Backward difference

As seen on equation (4.18) and equation (4.19) a small increment in the design variable $\rho_{el}^{(i)}$ is introduced. This is to check the sensitivity of the element by applying a small disturbance to the design variable, also called perturbation size. To determine the perturbation size for the forward and backward difference, a study of the sensitivity of a single design variable is performed. The analysis consist on calculating the forward and backward difference of the chosen design variable within the range of perturbation sizes seen on figure 4.18. This study was done by applying an incremental disturbance on the lower left element and checking the transmission loss for each increment, see figure 4.17.

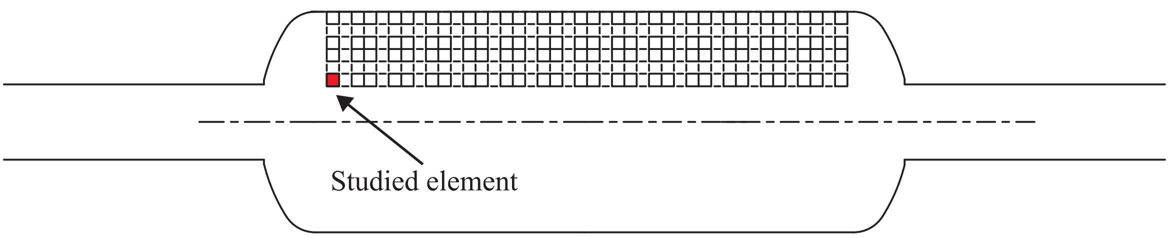

Figure 4.17: Chosen element for the perturbation size study.

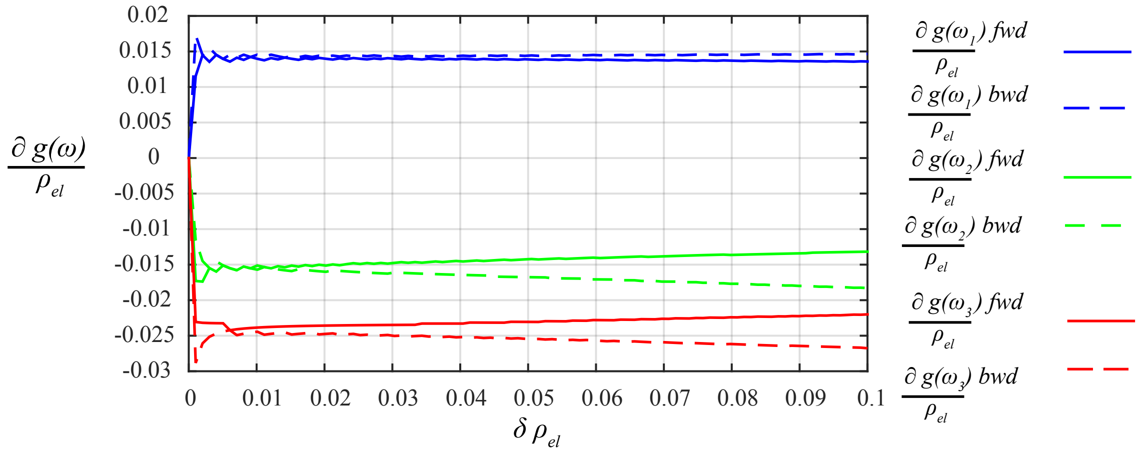

Figure 4.18: Constraint gradient tendency by the effects of $\delta\rho_{el}^{(i)}$ for each frequency.

Figure 4.18 show an unstable tendency of the curves at a very small increment of $\rho_{el}^{(i)}$. This is interpreted as numerical noise. Noise in the curves represent a rough line in the function curve. In the end of figure 4.18 it is observed that the forward and backward differences are separating from each other which indicates a non-linear, non-convex curve on a larger scale. To determine a good step size for the constraint gradient, a zoom of the interval [0, 0.02] was consider based on the findings of figure 4.18, seen on figure 4.19.

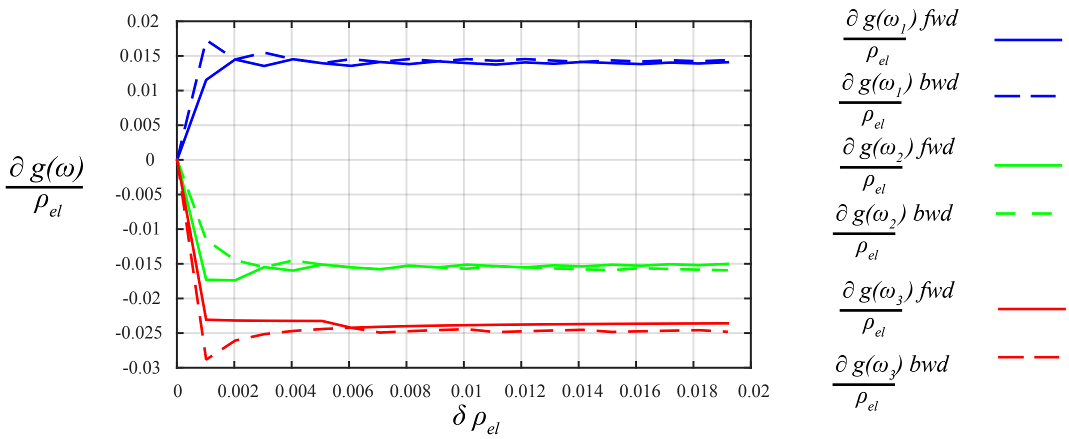

Figure 4.19: Zoomed view of constraint gradient tendency by the effects of $\delta\rho_{el}^{(i)}$ for each frequency.

Figure 4.19 gives a better view of the difference between forward and backward difference. A big difference can be seen where figure 4.18 predicted noise with a very small increment. However, both curves tend to equalize at a certain increment range. The increment was eventually chosen to be $\delta\rho_{el}^{(i)} = 0.01$ as the difference between forward and backward difference are similar for all three driving frequencies. It is important to note that ideally a new increment would be determined for every element for every iteration, but due to time constraints the increment is assumed to be sufficient for the whole analysis.

4.4.4 Merit function

When the design sensitivity is determined a new design variable can be determined using the *linprog* function in Matlab. The function solves the linear equation shown in

$$A\rho_c \leq b \tag{4.20}$$

Where the design variable has pre-set bounds ($\rho_c^{(LW)} < \rho_c < \rho_c^{(UP)}$).
When solving the linear problem to obtain a new design variable it may occur that the solver yields an infeasible design. To allow the solver to keep going without shutting off the optimisation process a merit function is introduced. The merit function introduces an artificial variable to the constraints in the system, seen on equation (4.21). The constraints are normalized to avoid scaling problems with the artificial variable.

$$\phi_g^{(j)}\left(\rho_c,y\right) = -\frac{TL\left(\omega_j\right)}{17} + 1 - y_j \leq 0 \tag{4.21}$$

Where j = 1,2,3. By applying the artificial variable to the constraint it allows the optimiser to close the gap of infeasibility of the linear equation by changing the value of y_j. To avoid the optimiser abusing the artificial variable, a penalty is applied to the objective function, show in equation (4.22).

$$\phi_o\left(\rho_c,y\right) = min \sum_{i=1}^{n_e} \rho_{el}^{(i)}\left(\rho_c\right) V_e^{(i)} + a \cdot \left(\sum_{j=1}^{n_g} c \cdot y_j + \frac{1}{2} \cdot y_j^2\right) \tag{4.22}$$

Where a is a scaling parameter which is set to the absolute value of the real objective function, at first iteration, which ensures a proper scaling throughout the analysis. c is a penalization parameter for the artificial variable. In [Svanberg, 2007] it is recommended to keep the penalization of the artificial variable reasonably large to ensure that $y_j = 0$ at the optimum, where a penalization of $c = 100$ seems to suit the reasonably large value. However, in [Sørensen and Lund, 2015] it is stated that a penalization of $c = 10$ is sufficient in most cases. The linear problem for the optimiser to solve has now changed to the following:

$$min \;\; \phi_o\left(\rho_c,y\right) = min \sum_{i=1}^{n_e} \rho_{el}^{(i)}\left(\rho_c\right) V_e^{(i)} + a \cdot \left(\sum_{j=1}^{n_g} c \cdot y_j + \frac{1}{2} \cdot y_j^2\right) \tag{4.23}$$

$$subject\ to \;\; \phi_g^{(j)}\left(\rho_c,y\right) = -\frac{TL\left(\omega_j\right)}{17} + 1 - y_j \leq 0) \tag{4.24}$$

Since the optimiser only reads gradients the gradients of the merit function needs to be determined. The merit gradients can be seen in the following equations

$$\frac{\partial\ \phi_g\,(x{,}y)}{\partial y_j} = -1 \tag{4.25}$$

$$\frac{\partial\ \phi_o\,(x{,}y)}{\partial y_j} = a\,(c + y_j) \tag{4.26}$$

Equation (4.25) and equation (4.26) is added to the respective gradient matrices for the real constraints and objective function. Now that the linear problem is guaranteed to be feasible the optimiser will never fail trying to determine a new design variable. However, an infeasible design may be determined. A tool to ensure that the functions are feasible a tool to ensure convergence needs to be applied.

4.4.5 Convergence filter

As mentioned, the merit function guarantees the linear problem to be feasible. However, a tool needs to be implemented to guarantee a stable convergence of the linear problem. A convergence filter was developed in [Ming Chin and Fletcher, 2001] from the experiments conducted in [Fletcher et al., 1998] which is simple to implement to the case at hand. The filters acts as a line search algorithm within a selected trust region. The filter determines if a new design variable should be accepted or rejected, by evaluating information from previous iterations. If the new design variable has been declined the filter will adjust its move limits and evaluates the new linear problem. A detailed flow chart of the filter can be found in [Ming Chin and Fletcher, 2001]. It is important to note that in the algorithm for this optimisation problem only the linear part of the filter is considered. Table 4.1 shows the parameters applied to the convergence filter during the optimisation of the muffler.

Convergence filter parameters				
u	γ	β	σ	δ
0.01	10^{-6}	$1-\gamma$	2γ	γ

Table 4.1: Parameters applied to the convergence filter.

Where u is a infeasibility limit predefined by the user. A smaller infeasibility limit will provide a better result but at a cost of more iteration needed for convergence. For an initial guess of full material $u = 0.01$ has been sufficient. To ensures that the optimiser will continue even if the result is infeasible the maximum infeasibility u can be increased. The optimiser will aim to yield a feasible solution, but might converge at a more infeasible solution than with a smaller infeasibility limit. The filter accumulate points by using the following equations.

$$h = max\left(0{,}\phi_g^n\right) \tag{4.27}$$

$$f = \frac{\phi_o^n}{\phi_o^0} \tag{4.28}$$

Where h is the *measure of infeasibility* and f is the *normalized value of the objective function* with respect to the initial function value. It is proven in [Ming Chin and Fletcher, 2001] that when the convergence filter eventually accepts a new design variable, or a convergence criteria where the change in design variable reaches a small tolerance, a KKT point has been determined. The only thing which needs to be defined for the convergence filter is the move limit strategy.

4.4.6 Adaptive move limit strategy

The adaptive move limit strategy is applied to the convergence filter where the move limit will change depending on a new design is accepted or rejected. If a design variable is rejected the move limit is simply reduced by half. Reducing the move limit by half has been sufficient in most cases. When a design variable has been accepted by the convergence filter the move limit is increased. However, oscillation of the design variable might occur and should be avoided. This is handled by reducing certain move limits. To determine if the design variables are oscillating the following procedure is applied, inspired from [Sørensen and Lund, 2015].

If $\left(Z_i^n - z_i^{n-1}\right) \neq 0$ **then**
$O_{sc} = \frac{\left(Z_i^{n-1} - z_i^{n-2}\right)}{Z_i^n - z_i^{n-1}}$
If $O_{sc} < 0$ **then**
$\Delta_i^{n+1} = 0.5$
else
$\Delta_i^{n+1} = 1.15$
end if
else
$\Delta_i^{n+1} = 1.15$

Where Δ_i^n is the move limit at n^{th} iteration, the O_{sc} variable tracks oscillation of the design variable and z_i^n is the bounds for all real design variables and is determined from equation (4.29) found in [Sørensen and Lund, 2015].

$$z_i^{n+1} \in \left[max\left(z_i^n - \Delta_1^{n+1},0\right), min\left(z_i^n + \Delta_1^{n+1},1\right)\right] \tag{4.29}$$

An initial move limit of 20% has proven sufficient and makes the optimisation process finish at a reasonable time. When a design variable is accepted by the convergence filter the move limit is increased by 15%. However, if the design variable is oscillating the move limit is reduced by 50%. By reducing the move limits when the design variables are oscillating stabilization of the design variable will occur faster. When a new design variable is determined the new function values are calculated and the process is repeated until the design is accepted as a minimum.

4.4.7 Convergence criterion

At a certain point in the optimisation process the change in design variable will decrease drastically and the functions are close to a minimum. A criterion is inserted to stop the optimisation process as the change in design variable is small. The convergence criteria is expressed in equation (4.30).

$$\sqrt{\frac{\left(\phi_0^{(n-1)}(x,y) - \phi_0^{(n)}(x,y)\right)^2}{\phi_0^{(n-1)}(x,y) + 1}} \cdot 100\% < \epsilon \tag{4.30}$$

The convergence tolerance has been set as 10^{-2} as lower tolerances were significantly increasing the number of iterations without showing significant change in discreteness. However, the optimisation runs in a continuous scheme where the steepness variable β and the penalization is increased. As convergence criterion is met, a new check is done by calculating the *Measure of Density Non-Discreteness*. If $M_{dnd} < 2\%$ the solution is accepted as discrete enough. However, if the convergence criterion is met but $M_{dnd} > 2\%$ a larger penalization and steepness is applied and the optimisation continues. This process continues until all defined penalization values and steepness values have been applied. The penalization values and steepness values can be seen in the following equations.

$$p = [1\ ,\ 4\ ,6]\ \text{ For SIMP} \tag{4.31}$$

$$p = [0\ ,\ 14\ ,62]\ \text{ For RAMP} \tag{4.32}$$

$$\beta = [20\ ,\ 40\ ,80]\ \text{ For Steepness of thickness filter} \tag{4.33}$$

The initial value of the steepness is set to 0.01 and the penalization is set to $p = 1$ until the first solution is found. This way the optimiser will not converge prematurely. When the optimiser has converged with a new β and penalization the measure of density non-discreteness is calculated again and continues until either $M_{dnd} < 2\%$ or the last entry in both penalization and steepness has been through the optimisation process. Note that the penalization and steepness values are checked individually and adding more values to the vectors is possible. In this work the optimisation process is stopped when all penalizations and steepness values has been tried even though $M_{dnd} > 2\%$. If a discrete solution is yet to be found post-processing of the results must be performed. A flow chart of the optimisation processes can be seen on figure 4.20. Note that the flow chart does not consider the continuation process and should only be treated as a visualisation of the basic concept of the optimisation processes.

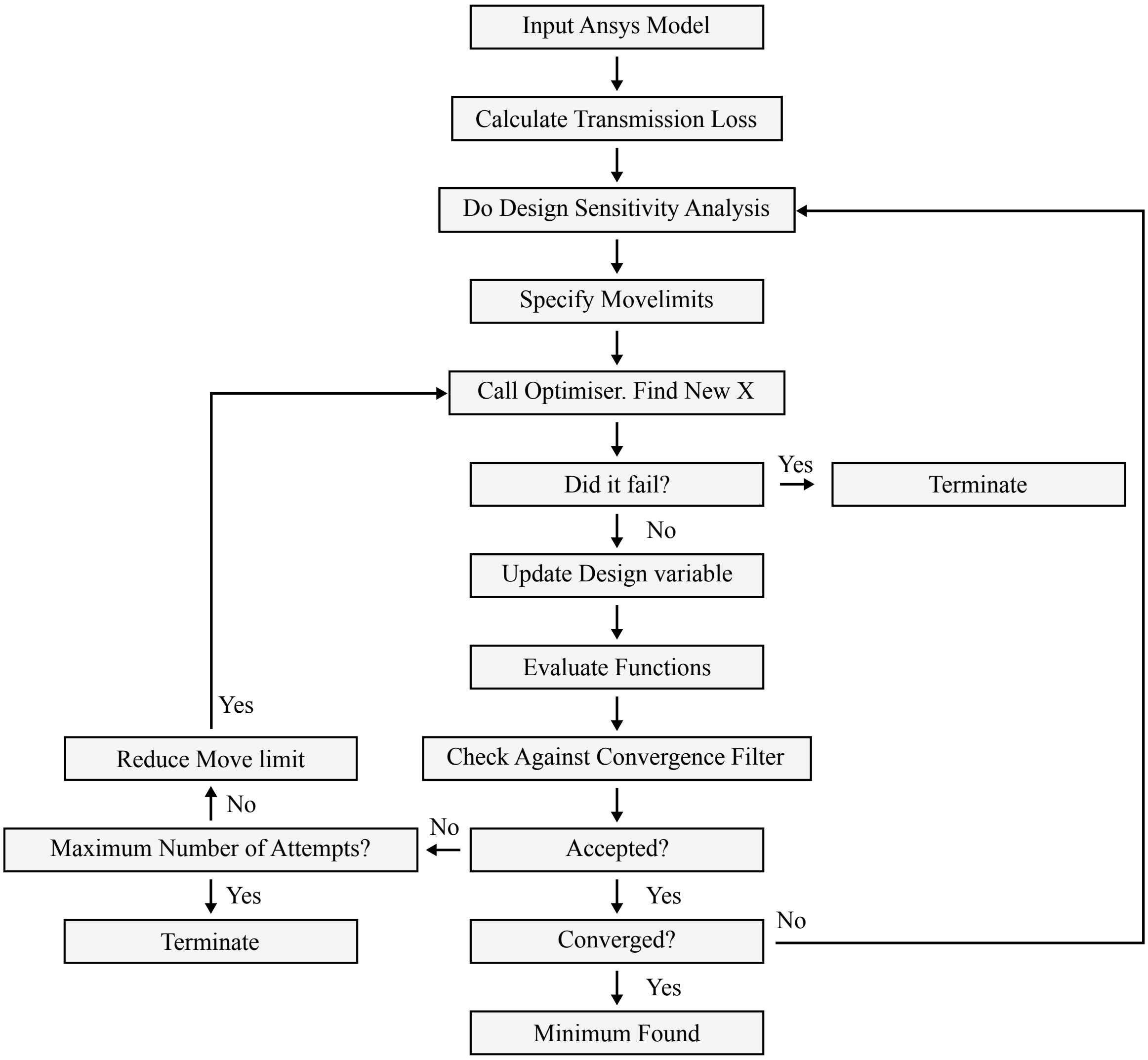

Figure 4.20: Flow chart of the optimisation routine.

5 Results and discussions

6 Conclusion

[1] Daniel Rey Romero Note!

[1] Daniel Rey
Romero Note: We could explain how LLoyd's Register can adapt the current optimization algorithm in order to include sound speed as a constraint, or maybe why not to do it because it would be computationally very expensive since we need to run ansys as many times as sound speed constraints we have.

Bibliography

Acoustic Guide, **2013**. ANSYS Acoustic Guide. *ANSYS Mechanical APDL Acoustic Analysis Guide*, 2013.

Fletcher, Leyffer, and L. Toint, **1998**. Roger Fletcher, Sven Leyffer, and Philippe. L. Toint. *On the global gonvergence of an SLP-filter algorithm. Numerical Analysis Report NA/183*. 1998.

Mehdizadeh and Paraschivoiu. Omid Z. Mehdizadeh and Marius Paraschivoiu. *A 3-D Finite Element Approach for predicting the Transmission Loss in Mufflers and Silencers with no Mean Flow*.

Ming Chin and Fletcher, **2001**. Choong Ming Chin and Roger Fletcher. *On the global gonvergence of an SLP-filter algorithm that takes EQP steps*. 2001.

Sigmund, **2007**. Ole Sigmund. *Morphology-based black and white filters for topology optimization*. Struct Multidisc Optim, 4, 2007.

Sorokin. Sergey V. Sorokin. *Lecture Notes on Machine Acoustics*.

Sørensen and Lund, **2015**. René Sørensen and Erik Lund. *Thickness filters for gradient based multi-material and thickness optimization of laminated composite structures*. Structural and Multidisciplinary Optimization, 2015.

Svanberg, **1987**. Krister Svanberg. *The Method of Moving Asymptotes - A New Method For Structural Optimization*. International Journal For Numerical Methods In Enginnering, 24, 1987.

Svanberg, **2007**. Krister Svanberg. *MMA and GCMMA - two methods for nonlinear optimization*. 2007.

Theory Reference, **2013**. ANSYS Theory Reference. *ANSYS Mechanical APDL Theory Reference*, 2013.

Venkataraman and Raj, **2014**. B. Venkataraman and Gokul Raj. *Experimental Investigation and Performance Evaluation of Passive Noise Control Components*. International Journal of Innovative Research in Science, Engineering and Technology, 3, 2014.

Wang, Stefanov Lazarov, and Sigmund, **2011**. Fengwen Wang, Boyan Stefanov Lazarov, and Ole Sigmund. *On projection methods, convergence and robust formulations in topology optimization*. Structural and Multidisciplinary Optimization, 43, 2011.

Wendt, D. Anderson Jr., G., Dick, and Grundmann, **1996**. John F. Wendt, John D. Anderson Jr., Degrez G., E. Dick, and R. Grundmann. *Computational Fluid Dynamics*. Springer, third edition edition, 1996.

Wu, Cheng, and Zhang, 2002. T.W Wu, C.Y.R Cheng, and P Zhang. *A direct mixed-body boundary element method for packed silencers*. J. Acoust. Soc. Am., 111, 2002.

Yoon, 2012. G.H. Yoon. *Acoustic topology optimization of fibrous material with Delany–Bazley empirical material formulation*. Journal of Sound and Vibration, 332, 2012.

Write here the first appendix A

Appendix-CD B